Mineralium Deposita (2024) 59:109–131
https://doi.org/10.1007/s00126-023-01196-6

ARTICLE

Hydrothermal apatite as a robust U–Th–Pb chronometer for the Carlin-type gold deposits in the Youjiang basin, SW China

Wei Gao[1] · Ruizhong Hu[1,2] · Yong Huang[1,3] · Jingjing Zhu[1] · Qiuli Li[4] · Lu Mei[1,2] · Xianwu Bi[1] · Jianzhong Liu[5]

Received: 2 November 2022 / Accepted: 16 July 2023 / Published online: 14 August 2023

Abstract

The formation of Carlin-type gold deposits is poorly constrained, mainly due to the lack of accurate ages for gold mineralization. The Youjiang basin, SW China, represents the world's second-largest Carlin-type gold province after NV, USA. In this paper, we use hydrothermal apatite U–Th–Pb dating to systemically determine the mineralization ages of five Carlin-type gold deposits, namely, Shuiyindong, Jinfeng, Zimudang, Linwang, and Jinya, in the Youjiang basin. The hydrothermal apatite is characterized by intimate intergrowth with gold-bearing sulfides, presence of primary fluid inclusions, irregular morphology and cathodoluminescence zoning, and MREE-enriched composition patterns, indicating that it is clearly associated and coeval with gold mineralization. The concentrations of lattice-bound U and Th in the apatite are highly variable, making it suitable for in situ secondary ion mass spectrometry (SIMS) U–Th–Pb dating. The dating results of hydrothermal apatite from the five deposits show that they formed at ca. 150–140 Ma, contemporary with the widespread felsic magmatism and associated W–Sn mineralization to the east of the Youjiang basin, probably in response to slab breakup of the Paleo-Pacific oceanic plate beneath the South China continental plate. Our case story suggests that hydrothermal apatite could be a robust chronometer for age dating of sedimentary rock-hosted gold mineralization worldwide.

Keywords Carlin-type gold deposits · The Youjiang basin · Hydrothermal apatite · U–Th–Pb dating · Geodynamic setting

Introduction

Since the Carlin-type gold deposits were discovered in NV, USA, and the Youjiang basin, SW China, this type of deposits has accounted for a significant proportion of the global gold supply and represents one of Earth's most important hydrothermal gold systems (Hu et al. 2017; Muntean and Cline 2018; Cline 2018). These deposits mainly occur as hydrothermal replacement orebodies hosted within calcareous sedimentary rocks and are characterized by wall-rock alteration of decarbonation, silicification, argillization, and sulfidation related to low-temperature (180–240 ℃), low-salinity, and acidic auriferous fluids (Hu et al. 2002; Cline et al. 2005; Su et al. 2009a). Gold primarily occurs as "invisible" lattice-bound Au or nanosized gold particles in disseminated pyrite that is invariably enriched in As, Sb, Hg, and Tl (Simon et al. 1999; Palenik et al. 2004; Reich et al. 2005; Liang et al. 2021). Gold-bearing arsenian pyrite commonly forms overgrowth rims on pre-ore barren pyrite cores (Barker et al. 2009a; Su et al. 2012; Xie et al. 2018). Despite of decades of research on the Carlin-type gold deposits, their

Editorial handling: B. Lehmann

✉ Ruizhong Hu
huruizhong@vip.gyig.ac.cn

✉ Yong Huang
huangyong@mail.gyig.ac.cn

1 State Key Laboratory of Ore Deposit Geochemistry, Institute of Geochemistry, Chinese Academy of Sciences, Guiyang 550081, China

2 College of Earth and Planetary Sciences, University of Chinese Academy of Sciences, Beijing 100049, China

3 Chengdu Center, China Geological Survey (Geosciences Innovation Center of Southwest China), Chengdu 610218, China

4 State Key Laboratory of Lithospheric Evolution, Institute of Geology and Geophysics, Chinese Academy of Sciences, Beijing 100029, China

5 Guizhou Bureau of Geology and Mineral Exploration & Development, Guiyang 550018, China

genesis and associated geodynamic processes remain enigmatic (Muntean and Cline 2018).

Precise and accurate dating of ore systems is critical in linking metal enrichment with specific tectonic events. It is the precondition to establish robust genetic models and effective exploration strategies (Rasmussen et al. 2006; Ehrig et al. 2021; McDivitt et al. 2022). However, constraints on timing are difficult to be achieved for Carlin-type gold deposits, largely due to the lack of unequivocally gold-related mineral geochronometers (Hofstra et al. 1999; Arehart et al. 2003). On the bumpy way of research on Carlin-type gold deposits in NV, significant dating efforts yielded a very wide age range of 158–10 Ma (Arehart et al. 1993). Not until the identification of hydrothermal galkhaite and adularia closely related to gold mineralization, the timing of Carlin-type gold deposits in NV was well constrained at ca. 42–34 Ma (Hofstra et al. 1999; Tretbar et al. 2000; Arehart et al. 2003). These reliable age dates decoded the geodynamic trigger of Carlin-type gold mineralization in NV, which was in response to the regional stress transition from contraction to extension due to rollback of the Farallon plate (Cline et al. 2005).

As the world's second largest Carlin-type gold province, the Youjiang basin of South China is endowed with numerous Carlin-type gold deposits, with proven reserves of over 1000 t Au (Su et al. 2018; Hu et al. 2017, 2020). There has been a long-standing controversy regarding the timing of mineralization and geodynamic setting. During the past decades, highly variable mineralization ages of 270 to 40 Ma have been obtained by various dating methods (Hu et al. 2017, and references therein). These dates were obtained either by indirect methods (e.g., quartz fission tracks, Zhang and Yang 1992; electron spin resonance dating, Liu et al. 2006) or by conventional bulk analyses of mineral separates (e.g., sulfides Re–Os, Chen et al. 2015; Ge et al. 2021; sericite Ar–Ar, Chen et al. 2009; calcite Sm–Nd, Su et al. 2009b). However, the equivocal relationships between the dated minerals and gold mineralization make these data highly questionable. For example, the gold-bearing pyrite is commonly characterized by core-rim growth textures that formed during temporally discrete events (Su et al. 2012; Xie et al. 2018; Gao et al. 2022). Therefore, dissolution-based Re–Os or Rb–Sr dating of pyrite may obtain mixing ages for gold mineralization and pre-ore sedimentary events. It is also difficult to identify the ore-stage calcite (Xie et al. 2018), as at the microscale individual calcite aggregates may have formed during several generations with significant time gap (Jin et al. 2021). Recently, in situ dating of hydrothermal monazite and rutile from two dolerite-hosted gold deposits yielded U–Th–Pb ages of ca. 214 and 144 Ma, respectively (Pi et al. 2017; Gao et al. 2021), suggesting two episodes of Carlin-type gold mineralization in the Youjiang basin (Hu et al. 2017). However, the dolerite-hosted deposits only constitute a small proportion of total gold reserves in the basin, and monazite and rutile are not identified in the typical sedimentary-hosted gold deposits. Thus, the temporal and spatial framework of Carlin-type gold mineralization at the basin scale remains unclear (Su et al. 2018; Wang et al. 2020).

It has been proven that apatite [$Ca_5(PO_4)_3(F, Cl, OH)$] can form from hydrothermal fluids in many ore-forming systems (Mao et al. 2015). Its crystallographic structure can accommodate REEs, Sr, halogens, and volatiles, making it a versatile tracer to monitor the source and evolution of ore-forming fluids (Zhao et al. 2015; Andersson et al. 2019; Palma et al. 2019; Cao et al. 2021). Hydrothermal apatite usually incorporates U and Th in μg/g concentrations and has a high closure temperature for the U–Th–Pb system (375–570℃ Cherniak 2010; Cochrane et al. 2014). With the considerable advancements of in situ U–Th–Pb dating techniques by laser ablation inductively coupled plasma mass spectrometry (LA-ICP-MS, Chew et al. 2011, 2014; Thompson et al. 2012, 2016) and/or secondary ion mass spectrometry (SIMS, Li et al. 2012), the feasibility of dating of common Pb-bearing apatite has been successfully demonstrated for many hydrothermal ore deposits (Cherry et al. 2018; Chen et al. 2019, 2022; Ma et al. 2021; Fox et al. 2021; Zhao et al. 2022). Hydrothermal apatite has been identified in ore-stage jasperoid and quartz veinlets in Carlin-type gold deposits of both NV and China (Hofstra et al. 1999; Hutcherson 2002; Chakurian et al. 2003; Barker et al. 2009b; Hill 2016; Chen et al. 2019), indicating that it could be a routine mineral for dating Carlin-type gold deposits.

In this study, hydrothermal apatite grains were identified from the five most representative Carlin-type gold deposits, namely, Shuiyindong, Zimudang, Jinfeng, Jinya, and Linwang, across the Youjiang basin. Petrographic observations of mineral paragenesis, textural and temporal relationships of apatite with gold mineralization, and apatite U–Th–Pb isotopic dating are comprehensively presented, which confirm that the Carlin-type gold deposits in the Youjiang basin mainly formed at ca. 150–140 Ma, contemporary with the widespread felsic magmatism and associated W–Sn mineralization to the east of the Youjiang basin. This study also suggests apatite as a robust chronometer for dating sedimentary rock-hosted gold deposits.

Regional geology

South China comprises the Yangtze and Cathaysia Blocks that were welded together along the 1500-km-long NE-trending Jiangnan Orogen at ca. 830 Ma (Fig. 1a, Zhao et al. 2011). It is separated from the North China Craton to the north and the Indochina Block to the southwest by the Triassic Qinling – Dabie Orogen and Ailaoshan – Song Ma

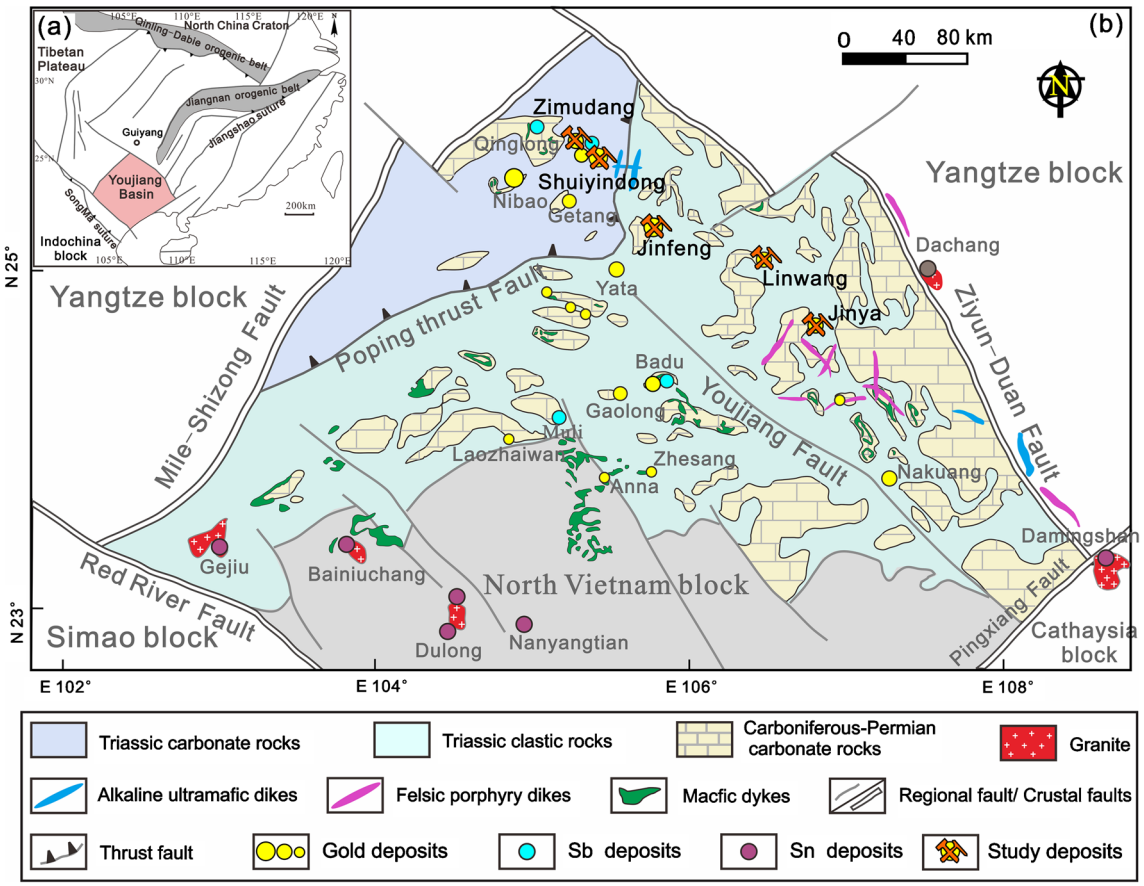

Fig. 1 **a** Simplified map showing tectonic units and adjacent regions of the South China Block. **b** Geologic map of the Youjiang basin showing the major Carlin-type gold deposits (modified from Gao et al. 2021)

suture, respectively (Hu et al. 2017). The Youjiang basin is located at the southwestern margin of South China and adjacent to the southwestern segment of the Jiangnan Orogen (Fig. 1a). It is bounded by the Mile – Shizong fault to the northwest and by the Ziyun – Yadu fault to the northeast, and separated from the Cathaysia and Indosinian Blocks by the Pingxiang – Nanning and Red River – Ailaoshan faults to the southeast and southwest, respectively (Fig. 1b).

Tectonically, the evolution of the Youjiang basin experienced three main stages (Cai and Zhang 2009; Du et al. 2013; Yang et al. 2012; Qiu et al. 2016): rifted basin developed at the southwestern margin of South China due to opening of the Paleo-Tethyan Ocean during the early Devonian, back-arc basin related to subduction of the Paleo-Tethys oceanic crust beneath South China during the early – middle Permian, and foreland basin due to closure of the Paleo-Tethys Ocean and subsequent collision between the South China and Indochina Blocks along the Ailaoshan – Song Ma suture during the Middle Triassic. Compression related to collision propagated northward into the Youjiang basin during the Late Triassic, forming NNW-trending thrusts and related fold systems, which were propagated NNE-ward, with NNE-ward Younging in the strata affected by deformation (Yan et al. 2006; Qiu et al. 2016; Yang et al. 2021). In the southern part of the basin, the deformation formed thick-skinned thrusts and upright fold that mainly affected the Early-Middle Triassic strata. In the northern tectonic unite, NNE-ward weakening stress formed thin-skinned thrusts and gentle folds that continued until the Early Jurassic (Yang et al. 2021). During the Middle-Late Jurassic, westward subduction of the Paleo-Pacific plate beneath South China formed NE-trending top-to-the-NW thrusting and fault-propagation folding in the Youjiang basin, which is superimposed on the Triassic NWW-trending structures, forming complex anticlines and domes (Qiu et al. 2016; Yang et al. 2021).

Stratigraphic units in the basin are dominated by Permian to Middle Triassic marine sedimentary rocks (Fig. 1b), with minor Cambrian to Devonian marine sequences being exposed at cores of some anticlines or domes. The basin witnessed several episodes of magmatic activities, including ca. ~ 260 Ma Emeishan' plume-related dolerite and basalt (Zhou et al. 2006; Fan et al. 2008), minor ca. ~ 84 Ma ultra-mafic dykes and ca. 100–94 Ma felsic dykes in the

northwestern and southeastern parts of the basin, respectively (Fig. 1b; Liu et al. 2010; Zhu et al. 2016). Recently, a few andesite and pegmatite dykes with ages of ca. 160–140 Ma were identified in southern of the basin (Li et al. 2013; Gan et al. 2020).

Deposit geology

The Youjiang basin hosts over 100 low-temperature hydrothermal gold deposits or occurrences clustering along NW- and NE-trending regional faults (Fig. 1b, Hu et al. 2002, 2017). These deposits have been shown to share characteristics comparable with the Carlin-type gold deposits in northern NV, USA (Hu et al. 2002, 2017; Su et al. 2009a, 2018; Xie et al. 2018; Gao et al. 2021). The estimated gold endowment is over 1000 tons, making the Youjiang basin the world's second-largest Carlin-type gold province worldwide (Hu et al. 2020). Two-thirds of the Carlin-type gold deposits occur in the southwestern Guizhou province, e.g., the giant Shuiyindong (263 t Au), Jinfeng (109 t Au), and Zimudang (75 t Au) deposits. Several large gold deposits occur in the northwestern Guangxi province, e.g., Jinya (> 35 t Au) and Linwang (30 t Au). These deposits are representative of various styles of gold mineralization and their ages can constrain the timing of Carlin-type gold mineralization in the Youjiang basin. To avoid repetition, only the features of the Jinfeng, Jinya, and Shuiyindong deposits are described below. The features of the Linwang and Zimudang deposits are provided in ESM 1, because they show characteristics similar to Shuiyindong and Jinfeng, respectively.

The Jinfeng deposit

Jinfeng, previously called Lannigou, is the second largest Carlin-type gold deposit with an average grade of 3.83 g/t or 0.12 oz/t in the Youjiang basin. Its geological features are summarized below, based on previous descriptions by Chen et al. (2011), Eldorado Gold Corp. (2011), and Xie et al. (2018).

The deposit is located on the eastern flank of the Laizishan anticline that involves Permian and Triassic strata in the mine area (Fig. 2a). The anticline is cut by a series of high-angle NW- or N-striking thrust faults (e.g., F_3, F_5, and F_6), which are variably displaced by younger NE-trending strike-slip faults (e.g., F_2 and F_{12}). NE-SW compression related to the Indosinian collision produced a complex series of tight to gentle folds and thrust faults, which are favorable for focused fluid flow (Ilchik et al. 2005). The exposed stratigraphy mainly consists of two distinct sequences (Eldorado Gold Corp 2011): shallow-water platform carbonate and deep-marine clastic rocks in the western and eastern parts, respectively. The former includes massive limestone of the Lower-Middle Permian Qixia and Maokou, Upper Permian Wujiaping, and Lower Triassic Luolou Formations. The latter is composed of mudstone, siltstone, and sandstone of the Middle Triassic Xuman, Niluo, and Bianyang Formations. No igneous rocks are reported in the mining field.

Gold mineralization is mostly controlled by the F_2, F_3, and F_6 faults, and occurs as veins and lenses hosted in dolomitic and calcareous siltstone, sandstone, and mudstone of the Xuman and Bianyang Formations (Fig. 2b). The main orebodies occur in dilation zones at the intersection of NW- and NE-striking faults (e.g., F_3 and F_2; Fig. 2b). The F_3 fault zone controls ~ 80% of the Au reserves and is characterized by high-grade ore with brecciated and stockwork textures.

The Jinya deposit

The Jinya deposit has an average grade of 3 g/t or 0.1 oz/t (China Geological Survey 2015). The deposit is located in the northeastern limb of the Bahe anticline that lies on the eastern margin of the Lingyun carbonate platform (Fig. 2c). The strata at Jinya also consist of two distinct sequences that have been folded, including massive limestone of the Upper Permian Heshan and Lower Triassic Luolou Formations in the east, and calcareous sandstone, siltstone, and mudstone of the Middle Triassic Baifeng and Hekou Formations in the west. The Baifeng Formation is divided into three units (unit 1–3) based on variable proportions of siltstone and mudstone. These strata were crosscut by N- to NW-trending major faults (e.g., F_1 and F_2) and secondary faults (e.g., F_3, F_5, and F_6).

The deposit consists of the Neilang and Nayuan ore blocks with 20 orebodies. Gold mineralization occurs as veins and lenses mainly hosted within dolomitic and calcareous siltstone and mudstone of the unit 2 of the Baifeng Formation, controlled by secondary faults and fracture zones between F_1 and F_2 faults (Fig. 2d). Ore is characterized by brecciated and stockwork textures.

The Shuiyindong deposit

Shuiyindong is the largest Carlin-type gold deposit in the Youjiang basin, with average grade of 5 g/t or 0.16 oz/t. The geology of this deposit has been described by Tan et al. (2015), Su et al. (2009a, 2018), and Xie et al. (2018). A brief summary is given here.

The deposit is located at the eastern part of the EW-trending and slightly N-verging Huijiabao anticline, which also contains the Zimudang gold deposits in its western part (Fig. 3a). The limbs of the anticline are cut by EW-striking and steeply dipping reverse faults (e.g., F_{101} and F_{105}), which

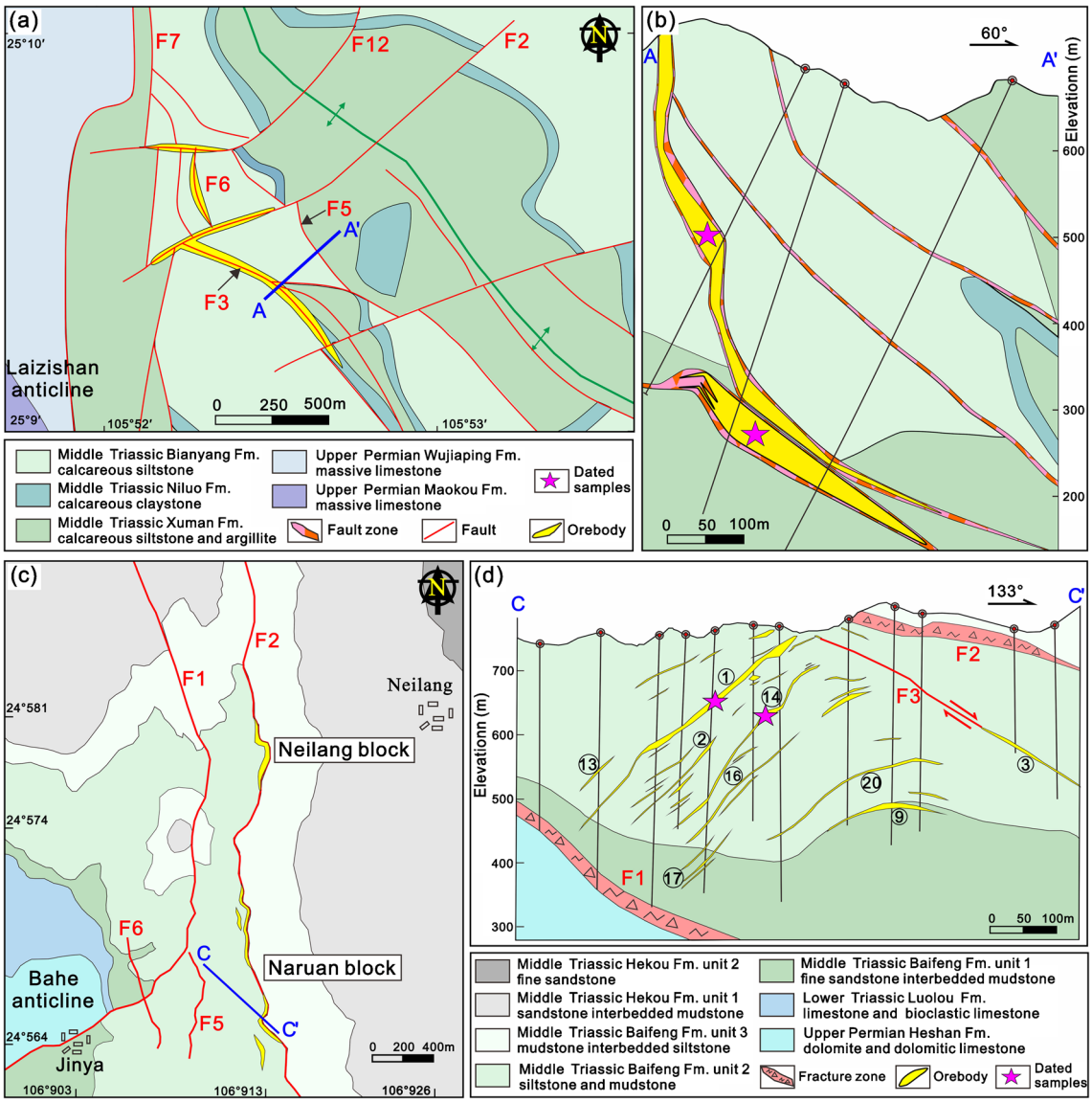

Fig. 2 **a** Simplified geologic maps and representative cross sections of the calcareous siliciclastic rock-hosted Jinfeng (**a**, **b** modified from Xie et al. 2018) and Jinya (**c**, **d** modified from Chen et al. 2015) deposits. Note the fault-bound nature of the orebodies

contain minor low-grade orebodies with realgar and orpiment (Su et al. 2009a). The anticline and reverse faults are further cut by a series of N- to NE-trending normal faults (e.g., F_{207} and F_{205}; Fig. 3a).

Sedimentary strata in the mining field are mainly composed of the Middle Permian Maokou; Upper Permian Longtan, Changxing, and Dalong; and Lower Triassic Yelang and Yongningzhen Formations (Fig. 3a), all of which have been gently folded. Gold mineralization mainly occurs as strata-bound orebodies hosted within bioclastic limestone, calcareous siltstone, and argillite of the Upper Permian Longtan Formation (e.g., nos. II, III, and IV; Fig. 3b), and the overlaying interbedded silty and bioclastic limestone of the Lower Triassic Yelang Formation (e.g., no. VIII). The Longtan Formation is about 300 m thick and can be divided into three units (1–3). Unit 1 is dominated by thick-bedded calcareous argillite. Unit 2 consists of thick-bedded silty argillite intercalated with thin bioclastic limestone and coal seams. Unit 3 is composed of thick-bedded calcareous siltstone and silty argillite intercalated with thin beds of bioclastic limestone. Orebodies in these strata are localized at structural highs along the hinge zone of the anticline (Su et al. 2018). Some low-grade orebodies (no. I; Fig. 3b) are hosted in silicified and breccia zones along the unconformity between the Longtan Formation and massive limestone of the Maokou Formation.

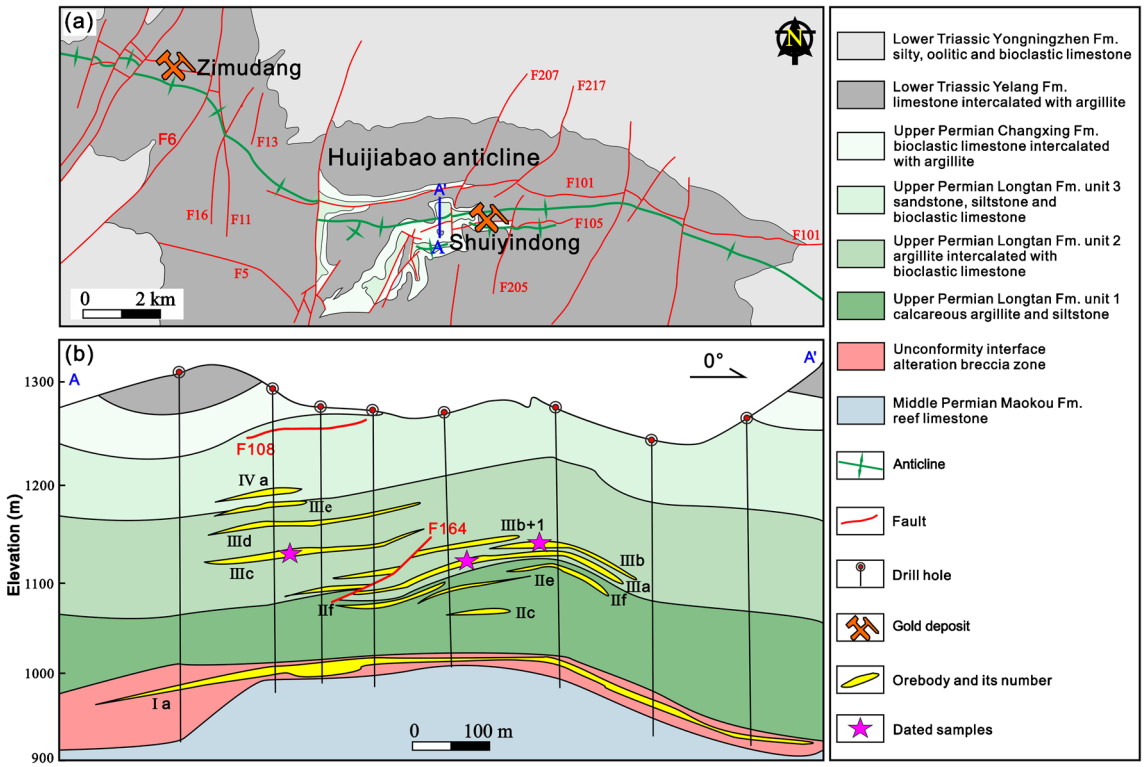

Fig. 3 Simplified geologic map (**a**) and representative cross section (**b**) of the bioclastic limestone-hosted Shuiyindong deposits (modified from Liu et al. 2006; Hou et al. 2016). Note the stratiform nature of the orebodies

Hydrothermal alteration and mineral paragenesis

Although the five deposits investigated here show various styles of mineralization, their paragenesis is similar. On the basis of petrographic comparison on sample transects with various grades, integrated with the overgrowth and crosscutting relationships relative to gold-bearing sulfides, the paragenesis is divided into pre-ore, ore, and late-ore stages.

Pre-ore stage Abundant Fe-bearing dolomite, calcite, and quartz, minor illite and muscovite, and trace sulfides and carbonaceous matter in the barren rocks represent the pre-ore stage mineral assemblages (Fig. 4a–c). Bioclasts in the limestone from Shuiyindong and Zimudang are also composed of calcite and Fe-bearing dolomite (Fig. 4c). Fe-bearing dolomite displays irregular and zigzag edges with numerous mineral inclusions of detrital quartz and muscovite (Fig. 4a). Pyrite, including framboidal and anhedral to euhedral variants, constitutes the dominant sulfide component in the barren rocks. This pyrite variant has no Au and is spatially unrelated to ore-stage alteration, and commonly forms cores on which gold-bearing pyrite was deposited in ore samples (Gao et al. 2022).

Ore stage Ore samples with moderate to high gold grades are distinguished by abundant disseminated pyrite and/or arsenopyrite (Fig. 4d–f), intimately associated with decarbonation, silicification, and argillization. Decarbonation is expressed by the dissolution of Fe-bearing dolomite and calcite. Hydrothermal quartz gradually replaces Fe-bearing dolomite and calcite (Fig. 4g–i). Where replacement was incomplete, Fe-bearing dolomite shows mosaic texture and irregular corroded grain boundaries, and is interstitial to quartz (Fig. 4g). Fe-bearing dolomite can be transformed to Fe-barren dolomite, both of which are encapsulated by hydrothermal quartz. Where replacement was complete, hydrothermal quartz exhibits reticulate texture and still contains tiny residual grains of Fe-bearing dolomite (Fig. 4i). The hydrothermal quartz is regarded as jasperoid, similar to that of Carlin-type gold deposits in NV (Cline 2001; Lubben et al. 2012). Two habits of jasperoid are identified, including (1) fine-grained and interlocking reticulate jasperoid (jsp-1) that replaced Fe-bearing dolomite (Fig. 4g–i). This jasperoid is common in all deposits in this study; (2) fine- to medium-grained jasperoid (jsp-2) that partially replaced fossil bioclasts in Shuiyindong and Zimudang (Fig. 4j, k). The jsp-2 occurs along the boundaries between ore matrix and voids resulting from replacement (Fig. 4j), or formed as silicified clasts by completely filling the voids (Fig. 4k), both of

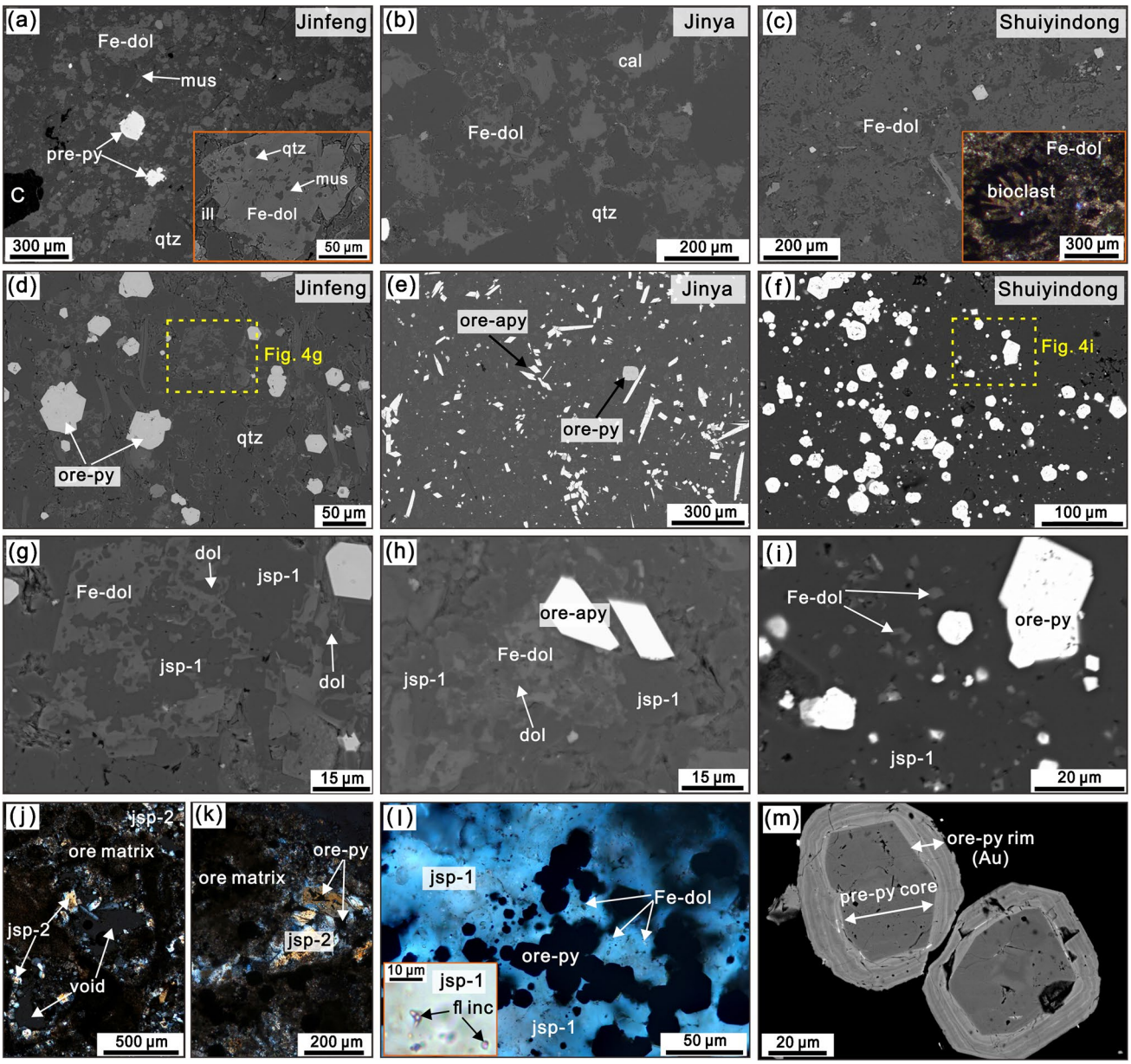

Fig. 4 Representative examples of low-grade host rocks (**a**–**c**) and medium- to high-grade ore samples (**d**–**m**) from Jinfeng, Jinya, and Shuiyindong. **a**, **b** Backscatter electron (BSE) images of calcareous siliciclastic hosts in Jinfeng and Jinya, respectively. The illustration shows the texture of Fe-bearing dolomite. **c** BSE image of carbonate host in Shuiyindong. The illustration shows the photomicrographs of morphology of bioclast. **d**–**i** BSE images of ore samples characterized by disseminated pyrite or arsenopyrite. Primary carbonate minerals have been gradually replaced by ore-stage jasperoid (jsp-1). Pyrite or arsenopyrite are disseminated in jasperoid and low-Fe dolomite replacement bodies. **j**–**k** Photomicrographs of jasperoid (jsp-2) that replaced fossil bioclasts and contains ore sulfides. **l** Pyrite enclosed within jsp-1 that has primary two-phase fluid inclusions. **f** Representative zoned pyrite showing ore-stage arsenian pyrite rim and preore-stage As-poor pyrite core. Abbreviations: cal, calcite; dol, dolomite; Fe-dol, Fe-bearing dolomite; ill, illite; jsp, jasperoid; mus, muscovite; ore-py, ore pyrite; ore-apy, ore arsenopyrite; pre-py, preore pyrite; qtz, quartz

which preserved the morphology of parental bioclasts. Both jasperoid habits contain residual carbonate inclusions and ore sulfides, and display two-phase aqueous fluid inclusions (Fig. 4l). Silicification is also expressed by the formation of replacement-style quartz veins that show intimate textural relationships with jsp-1 and ore sulfides.

Ore pyrite and/or arsenopyrite are disseminated in jasperoid and low-Fe dolomite replacement bodies (Fig. 4h, i), suggesting that they formed as a result of sulfidation of Fe released by Fe-bearing carbonate minerals (Su et al. 2009a). The original occurrence and size of Fe-bearing carbonate minerals control the textures and distributions of

ore jasperoid and sulfides. Overall, ore pyrite and/or arsenopyrite mainly cluster at jasperoid grain boundaries, or are enclosed within jasperoid and dolomite crystals (Fig. 4l). These textures indicate that ore-stage pyrite and/or arsenopyrite and jasperoid contemporaneously precipitated from auriferous fluids.

Under high-contrast backscatter electron (BSE) imaging, ore-stage pyrite forms 10- to 30-μm-wide rims overgrowing anhedral to euhedral pre-ore stage pyrite cores (Fig. 4m), or occurs as individual fine-grained euhedral grains with less than 5 μm in diameter. These individual grains show features similar to the rims, with compositional zoning of As concentration and consistently high contents of Au, As, Cu, Sb, Hg, and Tl (Xie et al. 2018; Li et al. 2020; Gao et al. 2022). LA-ICP-MS analyses yield up to thousands of μg/g of "invisible" Au in arsenian pyrite from Shuiyindong and Jinfeng (Hou et al. 2016; Xie et al. 2018; Li et al. 2020). Transmission electron microscope (TEM) results reveal that gold primarily occurs as "invisible" ionic Au in the crystal structure of arsenian pyrite, with minor native Au nanoparticles due to post-mineralization annealing of the arsenian pyrite (Liang et al. 2021). At Jinya, ore-stage arsenopyrite also contains variable concentrations of invisible gold (Yang et al. 2022).

Argillization, at the expanse of silicate minerals, e.g., detrital muscovite, formed minor to trace fine-grained illite that encompasses jasperoid and gold-bearing pyrite and/or arsenopyrite. However, it is difficult to distinguish ore-stage illite from that formed during sedimentary and diagenetic processes. Additionally, hydrothermal apatite is another important alteration product during fluid-rock interaction. It generally occurs within replacement-style quartz veins and jsp-2 and is intergrown with ore sulfides.

Late-ore stage Realgar and calcite, together with minor orpiment, stibnite, and euhedral quartz, constitute the late-ore stage minerals. They mainly fill fractures, vugs, and other open spaces, and crosscut or overgrow ore-stage minerals (Fig. 5). These late-ore stage mineral assemblages reflect the cooling and collapse of the ore-forming systems (Cline 2001; Cline et al. 2005; Xie et al. 2018).

Sampling and analytical methods

Sample preparation

Approximately 150 samples, from a larger set of carefully characterized drillcore and open pit samples, were selected from pervasively fractured and silicified zones that are spatially associated with medium- to high-grade intervals of the five deposits. The samples are characterized by hydrothermal veining. Sample locations and representative samples are shown in Figs. 2, 3, and 5, respectively.

Polished thin sections were made and then characterized via transmitted-reflected light, scanning electron microscopy with backscattered electron (SEM-BSE), and cathodoluminescence (CL) imaging. The paragenetic sequences of hydrothermal vein systems, and the textural and temporal relationships of hydrothermal apatite with respect to gold mineralization and vein generations, were carefully examined. Several apatite grains with high-contrast BSE or CL zoning and large size (> 200 μm in diameter) were selected to determine the distribution of minor and trace elements (e.g., U, Th, Pb, and REE) using LA- ICP-MS mapping, in order to guide apatite grains or regions with high U and Th concentrations and low common Pb compositions for further dating. After that, portions of polished thin sections containing selected apatite grains were extracted by micro-drilling and then mounted (25 mm) in resin together with apatite standards. All mounts were again characterized using transmitted, reflected light photomicrographs and SEM-BSE to accurately fix the location of apatite and to guide the placement of SIMS spots. After SIMS dating, the same analysis spots were analyzed by LA-ICP-MS to obtain the trace element concentrations. Apatite zones free of mineral inclusions and microfractures were chosen.

In-situ trace element analysis by LA-ICP-MS

In situ trace element analyses of apatite were conducted using a GeolasPro 193 nm ArF excimer laser ablation system coupled to an Agilent 7900 type ICP-MS at the State Key Laboratory of Ore Deposit Geochemistry (SKLODG), Institute of Geochemistry, Chinese Academy of Sciences (IGCAS). Analyses were performed with a laser beam size of 32 μm, a repetition rate of 6 Hz, and an energy density of 4 J/cm^2. The analytical and calibration procedures are provided in ESM 2.

Trace element mapping by LA-ICP-MS

Trace element mapping of apatite was performed using a RESOlution S-155 193 nm laser ablation system coupled to an Agilent 7700 × type ICP-MS at the SKLODG, IGCAS. The analytical procedure is similar to that of Ulrich et al. (2009) and summarized in ESM 2. Analytical parameters in this study are a beam size of 10 μm, scanning speed of 10 μm/s, energy density of 5 J/cm^2, and repetition rate of 10 Hz. The glass standard NIST610 was used for external calibration and the theoretical value of ^{40}Ca in apatite was used as internal standard.

High-resolution focused ion beam-scanning electron microscope (FIB-SEM)

High-resolution cross section imaging of apatite domains that include alternate CL-dark and CL-light bands was

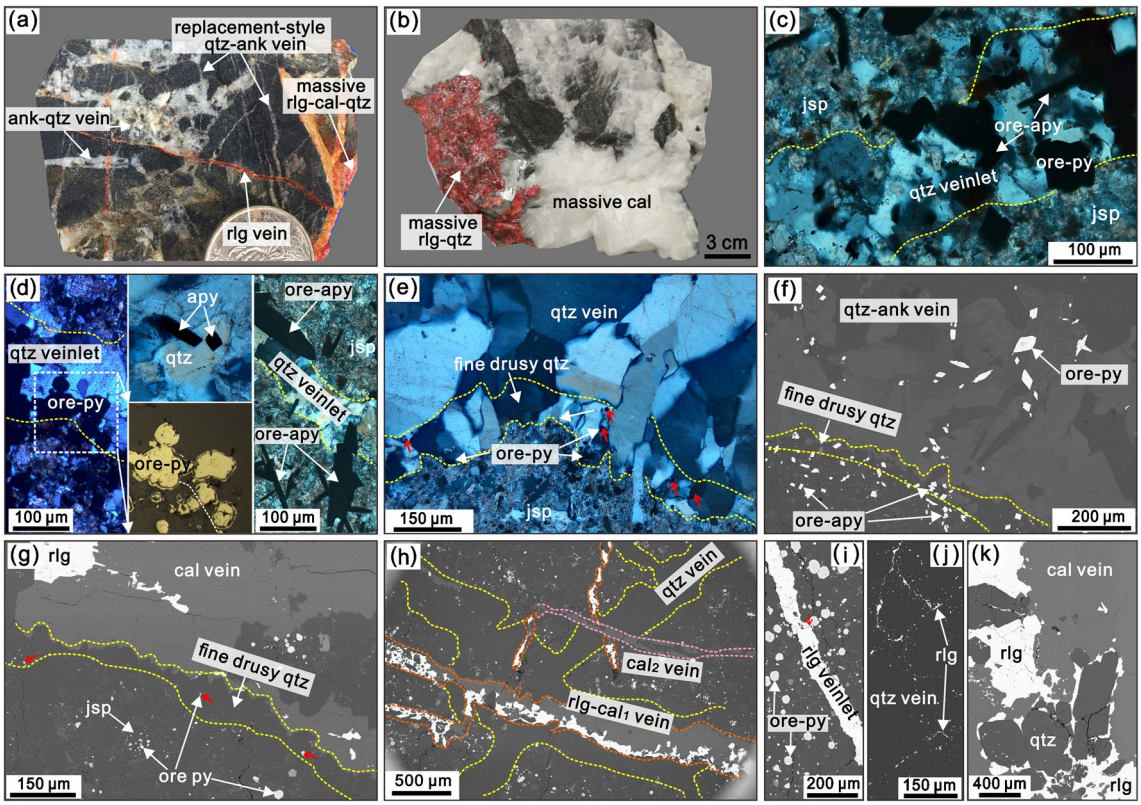

Fig. 5 Photographs (**a**, **b**), photomicrographs (**c**–**e**), and BSE images (**f**–**k**) of hydrothermal vein systems showing their modes of precipitation, mineral associations, and paragenetic sequences. **a**, **b** Three vein types including replacement-style quartz veins, cemented-style or fracture-infill calcite-realgar-quartz veins, and massive realgar-calcite-quartz aggregate. **c** Replacement-style quartz veinlet containing ore sulfides and crosscutting the masses of ore jasperoid and sulfide. **d** Ore sulfides in replacement-style quartz veinlets, showing contemporaneous precipitation of veinlet quartz and ore sulfides. **e**, **f** Masses of ore jasperoid and sulfides rimmed by fine euhedral quartz crystals and overgrown by vein quartz. Note that gold-bearing sulfides occur at the base of drusy quartz (designated by the red arrows). Vein quartz conforms to the crystal terminations of drusy quartz. **g** Massive calcite encompassing fine euhedral quartz that rims the masses of ore jasperoid and pyrite. Note that calcite conforms to euhedral crystal terminations of drusy quartz and is further overgrown by realgar. **h** Hydrothermal vein systems with overgrowth and crosscutting relationships. **i** Late-ore stage realgar vein crosscutting masses of ore jasperoid and sulfides. **j** Late-ore stage realgar vein along fractures of replacement-style quartz vein. **k** Massive realgar-calcite-quartz assemblage. Realgar overgrows calcite and euhedral quartz crystals. Ore sulfides are absent in the massive assemblage. Abbreviations: ank, ankerite; cal, calcite; jsp, jasperoid; ore-py, ore pyrite; ore-apy, ore arsenopyrite; qtz, quartz; rlg, realgar

conducted using a FEI Scios dual-beam (FIB-SEM) system at IGCAS. The foil was extracted in situ from polished thin sections using a focused ion beam (FIB) following the FEI Scios dual-beam methods. After extraction, samples were attached to the copper grid using Pt deposition. The section was thinned to less than 100 nm to reduce the analytical artifact.

In-situ U–Th–Pb dating by SIMS

In situ apatite U–Th–Pb isotope analyses were conducted using a Cameca IMS-1280HR SIMS at the Institute of Geology and Geophysics, Chinese Academy of Sciences in Beijing, China. Detailed descriptions of instrumental parameters and analytical procedures have been described by Li et al. (2012). An O^{2-} primary ion beam was accelerated at 13 kV, with an intensity of ~ 10 nA. The ellipsoidal spots are about 20 × 30 μm in size. A mass resolution of ~ 9000 (defined at 50% peak height) was used to separate $^{40}Ca_2{}^{31}P^{16}O_3{}^+$ peaks from isobaric interferences. A single-electron multiplier was utilized to measure the secondary ion intensities by peak jumping mode. Each measurement consists of 10 cycles and the total analytical time is ca. 15 min. Prior to analysis, pre-sputtering of the primary ion beam over each target area was used to reduce the contribution from surface Pb to insignificant levels. Detailed analytical and calibration procedure and common-Pb correction methods are supplied in ESM 2.

Hydrothermal vein systems

The samples selected for dating are characterized by hydrothermal vein systems with mature overgrowth and crosscutting textures. Three discrete types of hydrothermal vein and their paragenetic sequences are distinguished based on the mode of precipitation, mineral association, and spatial relationship with ore-stage jasperoid and sulfides (gold-bearing pyrite or arsenopyrite). They include replacement-style quartz veins, cemented-style or fracture-infill calcite-realgar-quartz veins, and massive realgar-calcite-quartz aggregates (Fig. 5a, b).

Replacement-style quartz veins Mineralized rocks with ore-stage jasperoid and sulfides are crosscut by replacement-style quartz veins (Fig. 5a). Under optical microscope and BSE images, quartz has two modes of precipitation, veinlet style and coarser vein style. The veinlet quartz is commonly less than 200 μm in width and composed of homogeneous, interlocking, subhedral to euhedral quartz crystals with 10 to 50 μm in diameter (Fig. 5c, d). The coarser vein quartz is more than 500 μm in width and consists of fine euhedral drusy quartz that coats the masses of ore-stage jasperoid and sulfides, and coarser quartz that overgrows drusy quartz (Fig. 5e, f). Fine drusy quartz crystals adhering to the masses of ore-stage jasperoid and sulfides are elongated, ranged between 50 and 200 μm in length, and coarsen in the direction of growth (Fig. 5e). Locally, some drusy quartz crystals grow across the contacts with the masses of ore-stage jasperoid and sulfides (Fig. 5e). The coarse quartz overgrowing drusy quartz displays more equant morphology and conforms to the crystal terminations of drusy quartz. Some debris of jasperoid with Fe-bearing carbonate inclusions is enclosed at the base of veinlets and fine drusy quartz, indicating the presence of open spaces during Fe-carbonate dissolution and jasperoid precipitation, similar to the observations by Cline (2001) in the Carlin district of NV.

Both veinlet quartz and fine drusy quartz contain variable amounts of ore-stage sulfides (gold-bearing pyrite and/or arsenopyrite), especially at their base along the contact with the masses of ore-stage jasperoid (Fig. 5d–f). Ore-stage sulfides along the contacts commonly grow across quartz and jasperoid or penetrate into the masses of ore-stage jasperoid (Fig. 5d). Ore-stage sulfides in the interior of veinlet and drusy quartz are intergrown with quartz (Fig. 5d). These spatial associations suggest temporal overlap of replacement-style quartz and gold mineralization. Locally, ore-stage sulfides are also enclosed by coarse quartz (Fig. 5f), especially adjacent to the contact with drusy quartz. However, the amount of sulfides decreases with distance away from the contact, with ore sulfides being typically absent in the younger coarse quartz. The coarse quartz conforms to the crystal terminations of drusy quartz (Fig. 5e, f) and is overgrown by late ore-stage calcite and realgar (Fig. 5g), demonstrating that at least some coarse quartz precipitated near the end of gold mineralization.

In summary, veinlet quartz and fine drusy quartz show intimate textural relationships with ore-stage jasperoid and contain variable amounts of gold-bearing sulfides, suggesting that they have a close temporal relationship. Therefore, replacement-style quartz veins probably formed during, or at least at the end of, ore-stage jasperoid and sulfide precipitation. They are penecontemporaneous with gold mineralization.

Cemented-style or fracture-infill calcite-realgar-quartz veins Carbonate dissolution, faulting, and local increase of hydraulic pressure may have brecciated the mineralized rocks and replacement-style quartz veins, generating more abundant fractures and larger open spaces. These fractures and open spaces can be filled by calcite, ankerite, realgar, and minor coarse euhedral quartz (Fig. 6a). Although calcite and ankerite are associated with realgar, calcite temporally predates realgar as observed at the microscale (Fig. 5g). Locally, the paragenetic sequence includes first the formation of a calcite vein, followed by realgar, and then succeeded by a second generation of calcite (Fig. 5h). Realgar commonly forms overgrowths on or encompasses calcite or fills pores and fractures of calcite (Fig. 5g). It also forms individual veins or veinlets crosscutting mineralized rocks (Fig. 5i), or occurs as stringers filling the fractures of ore-stage replacement-style quartz veins (Fig. 5j). It is noticed that calcite and realgar commonly conform to, and perfectly preserve, the euhedral crystal terminations of ore-stage fine drusy quartz (Fig. 5g), indicating the lack of chemical dissolution and physical abrasion. Such successive growth and overgrowth textures suggest that calcite and realgar closely followed ore-stage minerals and progressively precipitated from a single, evolving hydrothermal system during the late-ore stage.

In some localities where realgar is in contact with ore-stage jasperoid, realgar encloses ore-stage sulfides (Fig. 5i). Massive realgar distal from the contact is free of ore-stage minerals. Overall, these calcite-realgar veins have weaker spatial association with ore-stage jasperoid and gold-bearing sulfides, and replacement-style quartz veins terminate against these younger minerals (Fig. 5a), suggesting that calcite-realgar veins represent the late-ore stage minerals.

Massive realgar-calcite-quartz aggregates Locally, coarse realgar intergrown with quartz, together with coarse and euhedral calcite, occurs as massive assemblages within vugs and open spaces (Fig. 5b). At the microscale, calcite encompasses and conforms to euhedral quartz, both are further encompassed by realgar (Fig. 5k). Realgar also fills fractures

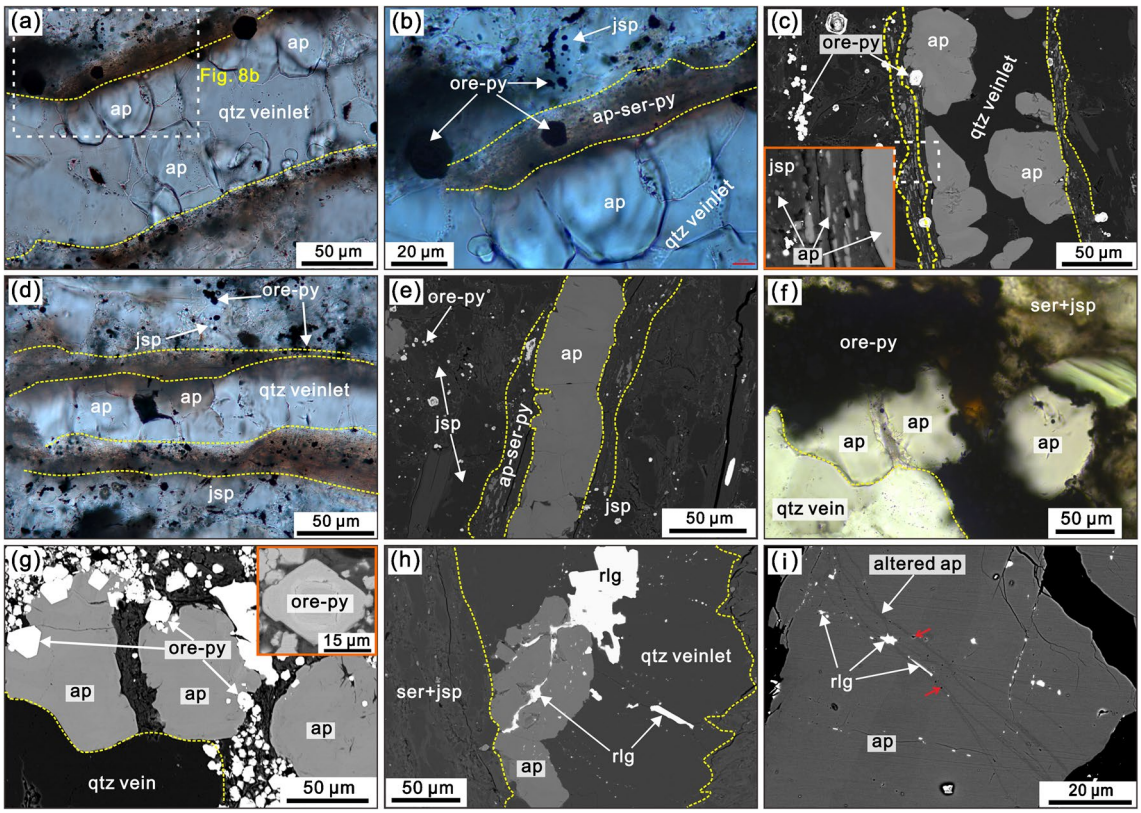

Fig. 6 Photomicrographs (**a**, **b**, **d**, and **f**) and BSE images (**c**, **e**, **h**, and **i**) of hydrothermal apatite in replacement-style quartz veinlet from Jinfeng. **a**–**c** Hydrothermal apatite occurring as anhedral and isolated or clustered grains that directly adhere to the masses of jasperoid and ore pyrite. Note the narrow accumulations of apatite-sericite-jasperoid-ore pyrite at the transitional contacts between the veinlet and masses. **d**, **e** Hydrothermal apatite in veinlet occupying the space between the masses of ore jasperoid and pyrite. Note the narrow accumulations of apatite-sericite-jasperoid-ore pyrite at the transition contacts. **f**, **g** Coarse hydrothermal apatite directly occurring in the wide accumulations of sericite-jasperoid-ore pyrite. **h** Hydrothermal apatite overgrown by late realgar. **i** Primary hydrothermal apatite crosscut by secondary altered apatite that is characterized by darked BSE imaging and numerous pores. Abbreviations: ap, apatite; jsp, jasperoid; ore-py, ore pyrite; qtz, quartz; rlg, realgar; ser, sericite

and pore spaces within and between euhedral quartz and calcite.

In summary, textural features and crosscutting relationships suggest that the vein and massive calcite, realgar, and minor quartz assemblages clearly postdate ore-stage jasperoid, gold-bearing sulfides, and replacement-style quartz veins. They formed as a result of cooling and collapse of the hydrothermal systems (Xie et al. 2018). However, these assemblages are found within and close to gold-bearing intervals. This clear spatial association with high-grade intervals provides a visual guide for gold mineralization (Tan et al. 2015).

Petrographic characteristics of hydrothermal apatite

Trace apatite, which shows textural characteristics of hydrothermal origin and synchroneity with gold mineralization, occurs within ore-stage replacement-style quartz veins containing gold-bearing sulfides. No apatite was observed in late-ore stage veined and massive calcite, realgar, and quartz.

Jinfeng and Linwang The apatite in replacement-style quartz veinlets occurs as isolated or clustered grains with generally

60 µm in diameter. They directly adhere to the masses of ore-stage jasperoid and pyrite, and grow toward the interior of open spaces (Fig. 6a–c). The remaining spaces are conformably filled by quartz. Apatite edges adhering to the masses of ore-stage jasperoid and pyrite are irregular and jagged (Fig. 6c). Apatite terminations in open space are conformed to quartz precipitated later (Fig. 6c). Apatite also forms veinlets occupying the space between the masses of ore-stage jasperoid and pyrite (Fig. 6d, e). Noticeably, narrow fine-grained apatite-sericite-jasperoid-ore pyrite accumulations occur at the transition zones between apatite-quartz veinlets and masses of ore-stage jasperoid and pyrite (Fig. 6c and e). Adjacent to the masses, very finely dotted apatite grains are enclosed in jasperoid (Fig. 6c). Where apatite-sericite-jasperoid-ore pyrite accumulations are wide, coarse apatite grains directly occur within them and show intimate intergrowth relationships with ore stage pyrite (Fig. 6f, g). Such textures suggest that the apatite formed synchronously with ore-stage jasperoid and pyrite, and grew in the open space created by carbonate dissolution or faulting. The apatite displays irregular sector CL zoning.

Late-ore stage realgar overgrows or occurs as infill on fractures in apatite (Fig. 6h), suggesting that the apatite formed earlier than realgar. Locally, primary apatite is crosscut by secondary apatite that is characterized by dark BSE image and numerous pores (Fig. 6i). Isolated, clustered, or beaded realgar is consistently distributed along the trails of secondary apatite or occupies the pores. Such textures suggest that primary apatite has locally been metasomatized by hydrothermal fluids related to realgar precipitation during the late-ore stage.

Jinya Apatite in replacement-style quartz-ankerite veins from Jinya is typically 20–100 µm in width and 200 µm in length, but locally has diameter up to 500 µm. Some apatite grains in veinlets adhere to the masses of jasperoid and ore arsenopyrite, grow toward the open spaces, and extend to the opposite side of the veinlets (Fig. S3a, d in ESM 3). Some apatite grains in veinlets grow from the interior of the masses of ore-stage jasperoid and arsenopyrite, and then grow into open spaces (Fig. S3b, e). These textures suggest that apatite formation accompanied the precipitation of ore-stage jasperoid and arsenopyrite, and that open spaces created by carbonate dissolution is in favorable for apatite growth. Some apatite grains also occur in coarse veins, where they share the same mineralogical and textural setting as ore-stage fine drusy quartz coating the masses of ore-stage jasperoid and arsenopyrite (Fig. S3c, f). In all occurrences, apatite is intergrown with arsenopyrite (Fig. S3d–f), further suggesting they are contemporaneous with each other. Late-ore stage realgar overgrows or occurs as infill on fractures in apatite (Fig. S3h). Additionally, apatite grains commonly contain primary two-phase fluid inclusions (Fig. S3c), consistent with those from ore-stage jasperoid or replacement-style quartz veinlets. Under CL imaging, apatite displays sector or band zoning (Fig. S3g).

Some apatite grains have experienced hydrothermal alteration, forming zones with dark BSE patterns that overprint the primary apatite. The altered areas occur as irregular intersecting patches. They exhibit sharp boundaries with the unaltered zones and display nano- and micro-porosity (Fig. S3h). These textural features are consistent with secondary alteration of apatite via dissolution-reprecipitation processes (Harlov 2015). The development of altered areas has a close spatial association with realgar, comparable with that in Jinfeng.

Shuiyindong and Zimudang Apatite from Shuiyindong and Zimudang occurs within ore-stage jasperoid (jsp-2) formed by replacement of fossil bioclasts or within replacement-style quartz veinlets (Fig. S4 in ESM 3). The jsp-2 variant preserves the morphology of bioclasts and contains gold-bearing pyrite and sericite. Some tiny residual solid inclusions of Fe-bearing carbonate occur at the base of jsp-2. The apatite shows equilibrium texture with jsp-2, is closely intergrown with gold-bearing pyrite, and is then overgrown or crosscut by realgar. Apatite in quartz veinlets displays similar features with those from Jinfeng. In both occurrences, apatite contains primary two-phase fluid inclusions and displays dark and sector CL zoning. No altered apatite grains or areas are observed under high-contrast BSE imaging.

Analytical results

Trace element geochemistry of hydrothermal apatite

The full LA-ICP-MS results of minor and trace elements in hydrothermal apatite grains are tabulated in ESM 4 Table A1. During analysis, we strictly choose primary apatite grains without secondary alteration to avoid the effect of fluid-mediated metasomatism on apatite chemistry. Also, secondary alterations zones in apatite are generally too narrow to be analyzed by LA-ICP-MS.

Apatite grains from the five deposits contain high and variable Sr (314–11,315 ug/g), Y (445–2755 µg/g), ΣREE (1544–4928 µg/g), Na (74–882 µg/g), Si (0–2056 µg/g), and Fe (187–340 µg/g) concentrations. Across the population, the total (REE + Y) concentrations strongly correlate with Na concentration, and apatite grains from Shuiyindong, Zimudang, and Linwang have generally lower (REE + Y) and Na concentrations than Jinya and Jinfeng (Fig. 7a). In contrast, the total (REE + Y + Na) concentrations show negative correlation with Sr concentrations within individual deposits (Fig. 7b). The U

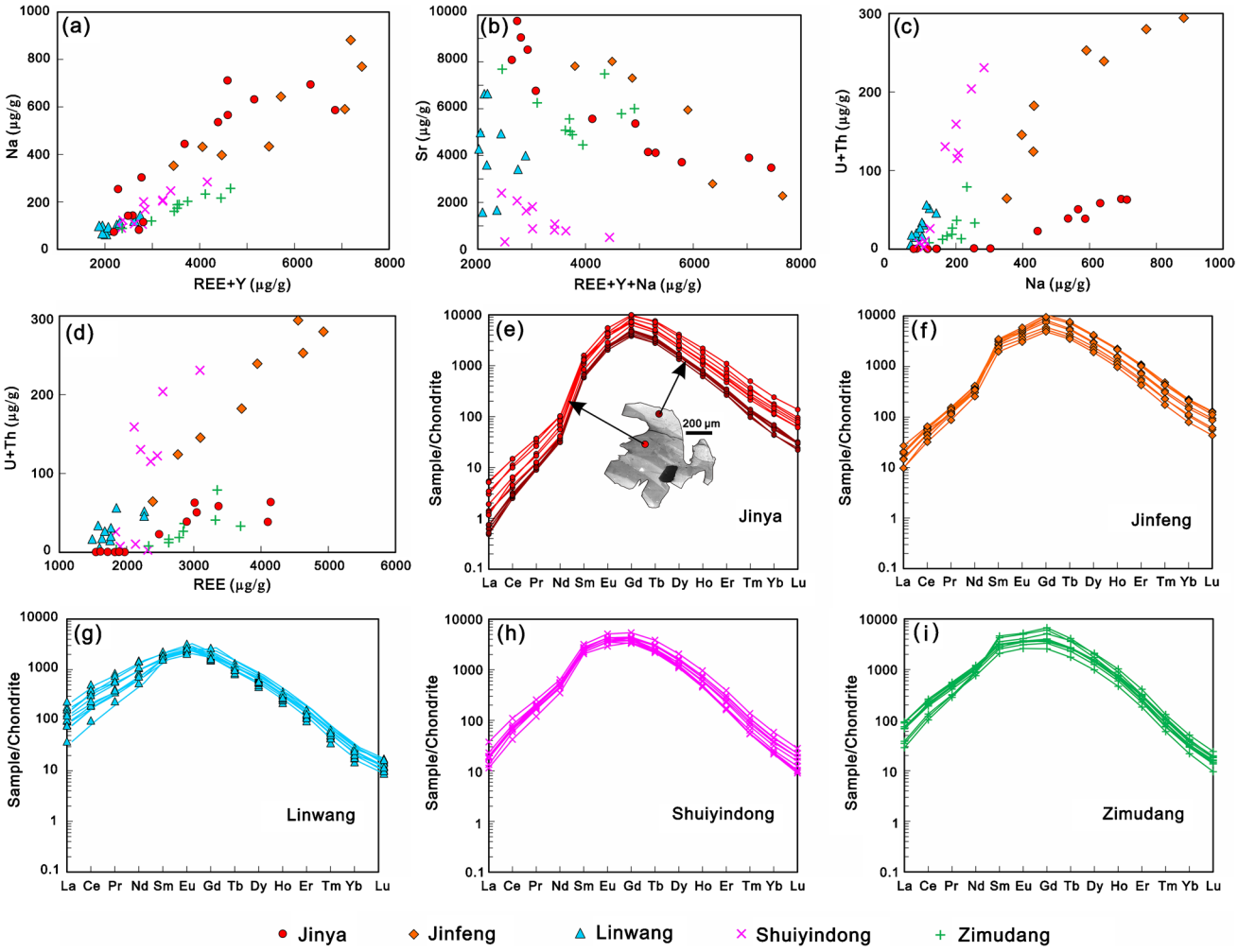

Fig. 7 **a–d** Variation plots of REE, Y, Na, Sr, U, and Th concentration of hydrothermal apatite. **e–i** REE concentrations normalized to chondrite values (Sun and McDonough 1989)

and Th concentrations in apatite are highly variable (U: 0.02–55 μg/g; Th: 0.04–230 μg/g). For individual deposits, the (U + Th) concentrations are positively correlated with Na as well as REE concentrations (Fig. 7c, d). Strikingly, all apatite grains contain particularly low Pb concentrations (mostly < 2 μg/g), with a positive correlation between (U + Th) and Pb concentrations, indicating that Pb was dominated by radiogenic Pb produced by U and Th decay.

The REE distribution patterns normalized to chondrite (Fig. 7e–i; Sun and McDonough 1989) show that all hydrothermal apatite grains from the five deposits are consistently characterized by enrichment of the middle rare earth elements (MREE), and depletion of the light and heavy earth elements (LREE and HREE). The calculated $(La/Sm)_N$ and $(Gd/Yb)_N$ ratios are 0.001–0.03 and 40–196, respectively. The REE patterns display weak Eu (Eu/Eu* = 0.78–1.3) and negative Ce (Ce/Ce^* = 0.52–0.82) anomalies.

Element mapping and high-resolution FIB-SEM observation of hydrothermal apatite

A hydrothermal apatite grain with large size (~ 600 μm in diameter) from Jinya was selected for in situ LA-ICP-MS mapping in order to reveal the relationship between CL zoning and element distribution (Fig. 8), particular for REE, U, and Th. The apatite grain appears homogeneous under high-contrast BSE imaging, but it exhibits irregular alternations of CL-bright and CL-dark bands (Fig. 8a). The CL zoning is accompanied by highly heterogeneous distributions of minor and trace elements (Fig. 8b–l). Compared to CL-bright bands, the CL-dark bands or areas contain markedly lower Sr, significantly higher Y, Na, and MREE (e.g., Sm and Eu), and slightly higher LREE (e.g., La and Ce) and HREE (e.g., Tm and Yb) concentrations. Noticeably, the CL-dark bands contain higher U (> 10 μg/g) and Th (> 1 μg/g) concentrations than those of CL-bright bands

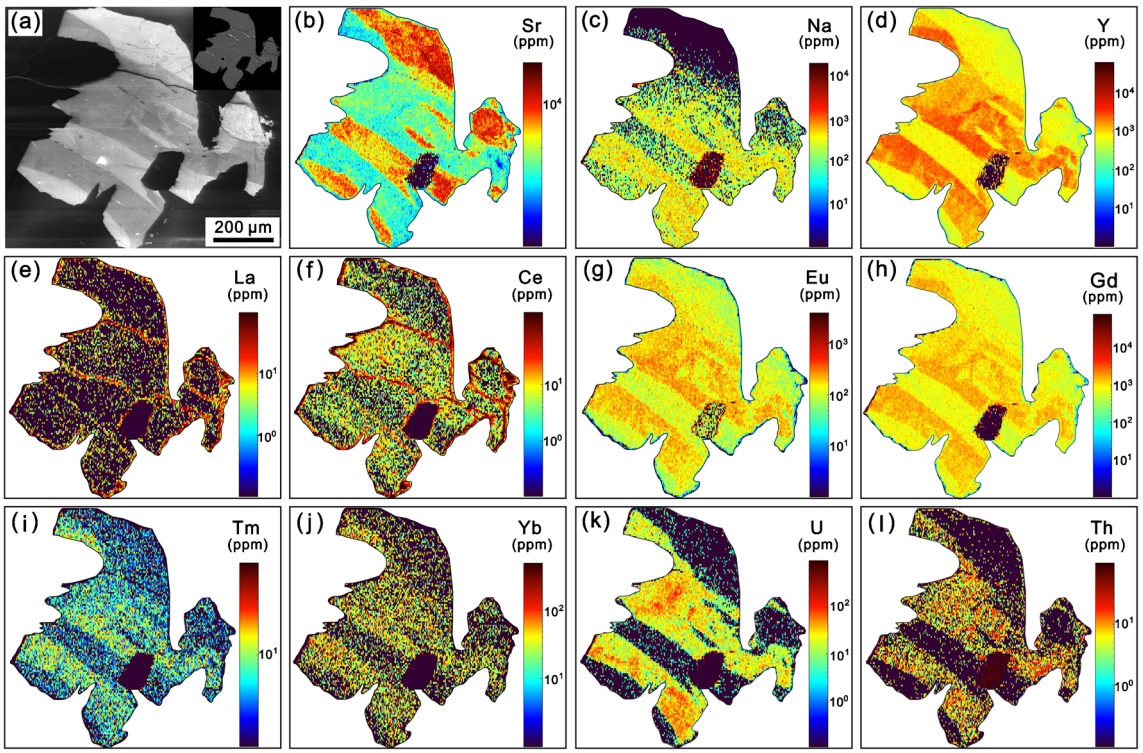

Fig. 8 CL image (**a**) and LA-ICP-MS qualitative element maps (**b–l**) of representative hydrothermal apatite from Jinya. The illustration in (a) shows the apatite has homogeneous BSE image

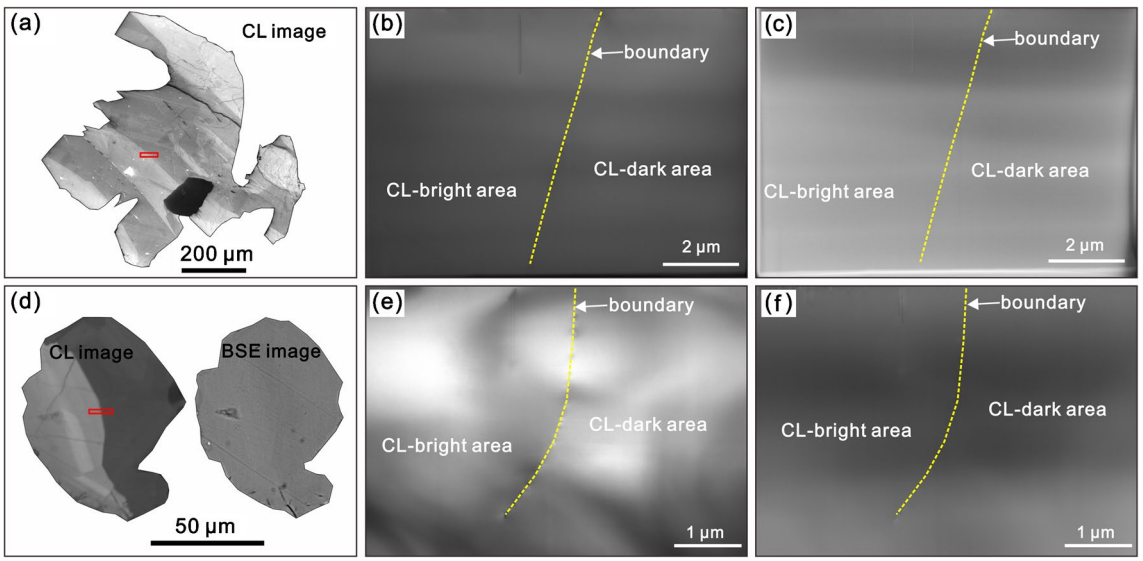

Fig. 9 **a**, **d** Representative apatite grains with different brightness of CL response. **b**, **c**, **e**, **f** High-resolution FIB-SEM images showing the areas with different CL imaging have homogeneous compositions. The locations of FIB foils are shown in a and d. **b**, **e** Bright field; **c**, **f** Dark field

(U < 1 μg/g, Th < 1 μg/g). However, both the CL-dark and CL-bright bands show consistent and tight REE distribution patterns (Fig. 7e).

Two representative FIB foils crosscutting the CL-dark and CL-bright bands and their boundaries from Jinya and Jinfeng, respectively, show that both bands are homogeneous and display consistent crystal structure (Fig. 9). No evidence of alteration or fluid metasomatism was observed. This suggests that the CL zoning resulted from the primary chemical difference rather than from secondary metasomatic

alterations, which was probably controlled by crystallization habit of apatite. No any U-, Th-, and Pb-rich inclusions were observed, suggesting the lattice-bound occurrence of U, Th, and Pb.

SIMS U–Th–Pb ages of hydrothermal apatite

The SIMS U–Th–Pb isotope data are presented in the ESM 4 Tables A2 and A3 and are graphically illustrated in Fig. 10. All reported ages are at the 95% confidence level. Below, the results and corresponding CL features of the analyzed apatite grains of each deposit are described.

Jinya We firstly dated the large apatite grain shown in Fig. 8, aiming to explore the effect of heterogeneous distribution of U and Th concentrations on the dating results (Fig. 10a). Highly variable U and Th contents and common Pb compositions (f_{206}) were recognized for the CL-dark and CL-bright bands. Eleven spots on the CL-bright bands contain low U (0.2–0.7 µg/g) and Th (0.0–0.2 µg/g) concentrations, yielding high f_{206} values of 81 to 100%. They plot close to the upper intercept on the Tera-Wasserburg Concordia. The 16 spots on CL-dark bands have high U (13–74 µg/g) and Th (3–37 µg/g) concentrations, yielding lower f_{206} values of 2.9 to 17.4% and plotting close to the lower intercept on the Tera-Wasserburg Concordia. The other two spots on the transitional area yield moderate U, Th, and f_{206}, and scattered along the regression line. All uncorrected 29 data spots define a good regression line and yield a lower intercept age of 145.0 ± 2.9 Ma (2σ, MSWD = 1.8), with the upper intercept of $^{207}Pb/^{206}Pb = 0.842 \pm 0.038$ for the common-Pb composition.

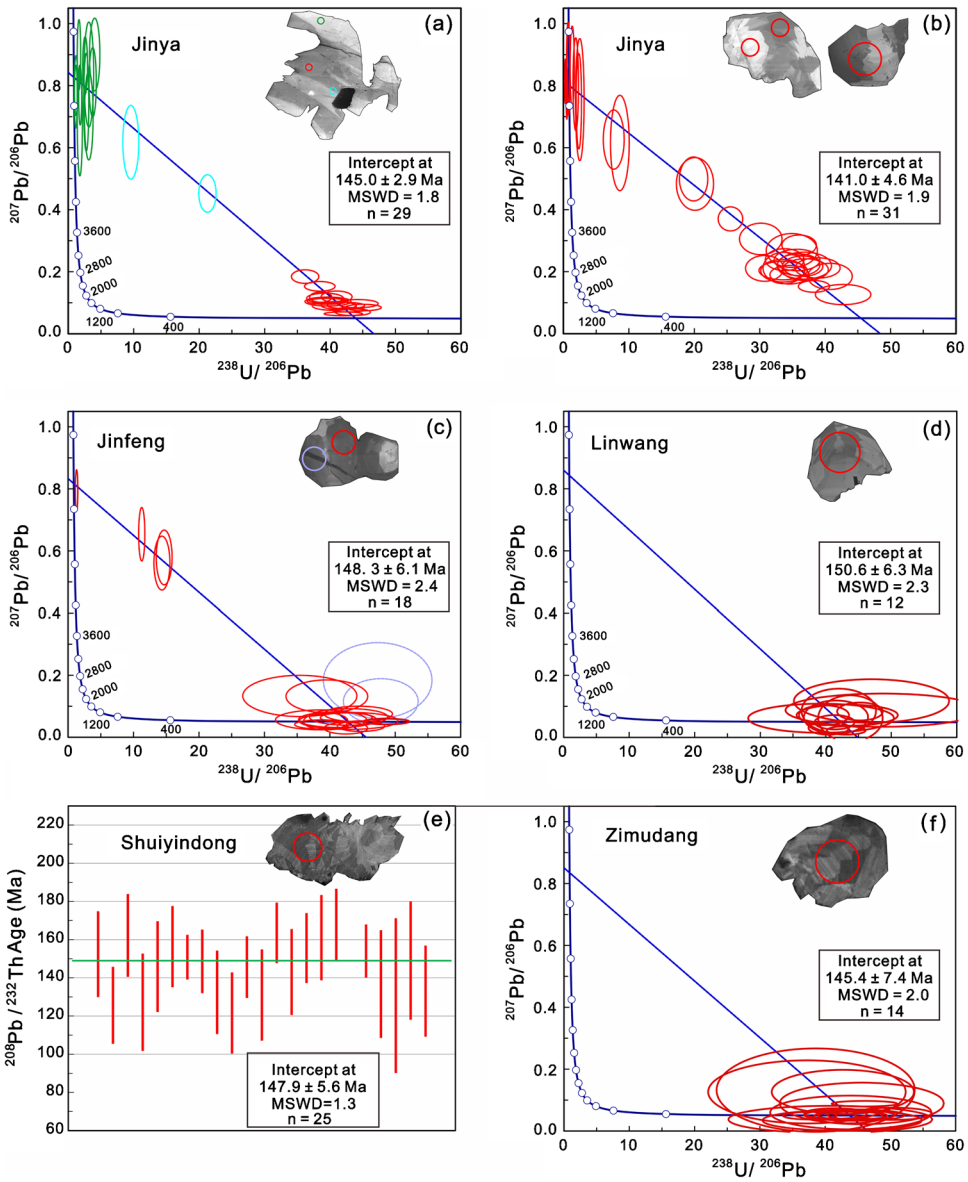

Fig. 10 Tera-Wasserburg U–Pb plots of hydrothermal apatite from Jinya (**a**, **b**), Jinfeng (**c**), Linwang (**d**), and Zimudang (**f**), and weighted mean corrected $^{208}Pb/^{232}Th$ age for hydrothermal apatite from Shuiyindong (**e**). The illustrations are representative CL images of dated apatite. The circle is 30 µm in diameter

The other 31 analyses were conducted on 23 apatite grains, with analyses containing variable proportions of CL-dark and CL-bright areas (Fig. 10b). The U and Th concentrations vary from 0.2 to 43 μg/g and 0.2 to 180 μg/g, respectively, with Th/U ratios of 0.1 to 11. Common Pb is also highly variable with f_{206} values ranging from 9.7 to 100%. The 31 data points on the Tera-Wasserburg Concordia define a well-constrained regression line and yield a lower intercept age of 141.0 ± 4.6 Ma (2σ, MSWD = 1.9), with an upper intercept of $^{207}Pb/^{206}Pb = 0.815 \pm 0.042$. The two ages are, within error, in good agreement with each other.

Jinfeng The hydrothermal apatite grains are generally less than 60 μm in diameter but occasionally up to 100 μm. Twenty-three analyses were conducted on 21 apatite grains. Three spots on bright-CL areas do not yield useful data due to their extremely low U (< 0.1 μg/g) and Th contents (< 1 μg/g). The remaining 20 spots covering variable proportions of CL-dark and CL-bright areas have highly variable U and Th contents of 1.3–47 μg/g and 2.3–298 μg/g, respectively, with Th/U values of 0.2–63. Among these, 18 spots have f_{206} values of 0.0–94% and define a good regression line on Tera-Wasserburg Concordia (Fig. 10c), with a lower intercept age of 148.3 ± 6.1 Ma (2σ, MSWD = 2.4) and an upper intercept $^{207}Pb/^{206}Pb$ of 0.833 ± 0.068. Two spots on secondary alteration areas plot to the right of the regression line and yield younger apparent ^{207}Pb-corrected ages, probably explained by minor radiogenic Pb loss during hydrothermal alteration (Kirkland et al. 2018; Fox et al. 2021).

Linwang The apatite grains are generally less than 60 μm in diameter and display dark CL images. Twelve analyses conducted on 12 apatite grains show relatively homogenous U (3.5–11.5 μg/g) and Th (0.0–1.6) contents, with Th/U ratios of 0.0 to 0.3. The values of f_{206} range from 0.0 to 8.6%. The measured data points plot in a tight cluster near the lower intercept on the Tera-Wasserburg Concordia (Fig. 10d), yielding a lower intercept age of 150.6 ± 6.3 Ma (2σ, MSWD = 2.3). The age was calculated from an assigned common Pb composition ($^{207}Pb/^{206}Pb = 0.845$), corresponding to the terrestrial Pb evolution model of Stacey and Kramers (1975).

Shuiyindong The apatite grains are generally less than 60 μm in diameter and have dark CL images. A total of 25 analyses were performed on 25 apatite grains. Among our dating attempts, these apatite samples are unique with their extremely low U (< 1 μg/g) but high Th (9–209 μg/g) contents and therefore very high Th/U ratios (52–1387, average = 311). Additionally, the ^{204}Pb-based f_{206} and f_{208} values are generally less than 1%. This makes Th–Pb dating feasible because of limited common-Pb contribution to the total ^{208}Pb (Chew et al. 2011; Li et al. 2012). The common-^{204}Pb corrected $^{208}Pb/^{232}Th$ ages yield a weighted mean age of 149.0 ± 6.0 Ma (2σ, MSWD = 2.0, Fig. 10e). Omitting three scattered spots, the weighted mean $^{208}Pb/^{232}Th$ age is 147.9 ± 5.6 Ma (2σ, MSWD = 1.3).

Zimudang The apatite grains have features similar to Shuiyindong. A total of 20 analyses were performed on 20 apatite grains. The apatite has variable U (0.8–112 μg/g) and low Th (0.1–20 μg/g) concentrations, with Th/U ratios of 0.01 to 3.4. The f_{206} values are 0.0–9.9% (mostly < 1%), indicating a low fraction of common Pb. All data points cluster near the lower intercept on the Tera-Wasserburg Concordia (Fig. 10f). Six points yielded high uncertainties of the U and Pb isotope ratios due to low U concentrations, and therefore were excluded to calculate the final age. Using an estimated common $^{207}Pb/^{206}Pb$ composition of 0.845 based on the terrestrial Pb evolution model (Stacey and Kramers 1975), a lower intercept age of 145.4 ± 7.4 Ma (2σ, MSWD = 2.0) was obtained for 14 spots.

Discussion

Hydrothermal origin and temporal relationship of apatite with gold mineralization

The apatite grains whose ages were determined in this study were from hydrothermally mineralized samples with jasperoid and gold-bearing sulfides (pyrite and/or arsenopyrite). They were only identified in replacement-style veinlet quartz and fine euhedral drusy quartz. The mode of precipitation, mineral association, and spatial relationship with ore-stage jasperoid and sulfides suggest that the veinlet quartz and fine drusy quartz formed during, or at least at the end of, the main ore stage. Similar replacement-style quartz that is penecontemporaneous with gold mineralization also occurs in the Carlin-type gold deposits of northern NV (Cline 2001; Lubben et al. 2012). The spatial distribution of apatite grains restricted to the ore-stage veinlet quartz and drusy euhedral quartz suggests that they have a close temporal relationship. Additionally, the apatite grains contain primary two-phase fluid inclusions that are comparable with those in ore-stage jasperoid and veinlet quartz (Zhang et al. 2003; Su et al. 2009a; Chen et al. 2018), further suggesting that they precipitated from the same hydrothermal fluids. More importantly, the apatite grains are closely intergrown with ore-stage gold-bearing sulfides, both of which are then overgrown or crosscut by late-ore stage calcite and realgar. These integrated petrographic data suggest that the apatite grains are hydrothermal in origin, and their formation is nearly contemporaneous with gold mineralization.

Geochemically, the apatite grains are characterized by striking enrichment of MREE and depletion of LREE and

HREE, which is different from that of detrital apatite in sedimentary rocks (Huang 2019). Previous works have suggested that ore-stage calcite, which is the most important gangue mineral of the Carlin-type gold deposits in the Youjiang basin, is characterized by its MREE-rich distribution pattern (Su et al. 2009a; Tan et al. 2015; Zhuo et al. 2019). By contrast, calcite unrelated to gold mineralization is enriched in LREE (Tan et al. 2015; Zhuo et al. 2019).

Interpretation of U–Th–Pb ages of hydrothermal apatite

In situ SIMS dating on hydrothermal apatite grains genetically related to gold mineralization from Shuiyindong, Jinfeng, Zimudang, Jinya, and Linwang yielded precise and reproducible U–Th–Pb ages of 150–140 Ma. These ages record the timing of gold mineralization for the following reasons.

Firstly, the lattice-bound occurrence of parent U and Th and daughter Pb in apatite is the precondition for U–Th–Pb isotope dating. In apatite, a large number of monovalent (e.g., Na^{+}), divalent (e.g., Sr^{2+} and Pb^{2+}), trivalent (e.g., REE^{3+} and Y^{3+}), and tetravalent (e.g., U^{4+} and Th^{4+}) cations can occupy the Ca site (Pan and Fleet 2002; O'Sullivan et al. 2020). The hydrothermal apatites from the Carlin-type gold deposits investigated here show strong positive correlations between (REE + Y) and Na concentrations, indicating a coupled substitution mechanism ($(REE+Y)^{3+} + Na^{+} = 2\,Ca^{2+}$) for the incorporation of these cations into the apatite lattices (Pan and Fleet 2002; Andersson et al. 2019; O'Sullivan et al. 2020). Similarly, total (U + Th) concentrations in the apatite exhibit positive correlation with Na and REE concentrations, indicating that parent U and Th could coherently substitute for the Ca site along with other cations with a range of ionic radii, e.g., REE^{3+} and Na^{+} (Pan and Fleet 2002; O'Sullivan et al. 2020). Radiogenic daughter Pb can also be accommodated in the original substitution site of U and Th, because Pb^{2+} occupies the Ca site (Pan and Fleet 2002). In addition, no U-, Th-, and Pb-rich mineral inclusions were observed under high-resolution FIB-SEM observations, further supported by the element mapping data and flat time-resolved depth profiles.

Secondly, the interpretation of apatite U–Th–Pb ages depends on the closure temperature of Pb diffusion in apatite and the thermal history experienced by the dated apatite. The estimated Pb-blocking temperatures of apatite range from 350 to 570 ℃ (Cherniak 2010; Cochrane et al. 2014; Chew and Spikings 2015). For the Carlin-type gold deposits in the Youjiang basin, the temperatures of hydrothermal fluids related to ore-stage Au and late-ore stage Sb–Hg mineralizations are 200–240 °C and 140–160 °C, respectively, based on microthermometric data of fluid inclusions (Zhang et al. 2003; Su et al. 2009a; Gu et al. 2012). Thermal history models suggest that the ore-host rocks have cooled below 150 °C since the Late Triassic (Qiu et al. 2016). All temperatures are significantly lower than apatite U–Th–Pb closure temperature range. Also, zircon fission track and U–Th/He dating suggest that no any thermal events with temperatures higher than 250 °C have affected the orebodies since their formation (Huang et al. 2019; Gao et al. 2021). Therefore, the hydrothermal apatite can immediately start its U–Th–Pb clock once formed, and post-crystallization redistribution or loss of daughter Pb isotopes by thermal effect can be ignored.

Thirdly, apatite is prone to post-crystallization fluid-induced modification or recrystallization (Harlov 2015). Minor hydrothermal apatite grains investigated in this study display alteration zones, e.g., apatite form Jinya and Jinfeng. These areas are characterized by dark BSE imaging, nano- and micro-porosity, irregular patches, and sharp boundaries with the unaltered zones, suggesting fluid-mediated post-crystallization modification via a dissolution-reprecipitation mechanism (Harlov 2015; Andersson et al. 2019; Palma et al. 2019). Additionally, the development of altered areas is closely associated with realgar and stibnite, indicating that the metasomatic event occurred during late-ore stage Sb–Hg mineralization. The successive growth and overgrowth textures between late-ore stage calcite-realgar-stibnite and ore stage fine euhedral drusy quartz suggest that they progressively precipitated from a single, evolving hydrothermal system, with no significant time gap (Cline 2001; This study). Therefore, metasomatism and alteration of apatite occurred shortly after its primary crystallization. However, the analyzed spots on alteration areas yielded highly dispersed data trending towards younger ages, indicating open-system behavior of U, Th, and Pb during metasomatic processes. We have carefully avoided the alteration zones during SIMS or LA-ICP-MS analyses for excluding the effect of metasomatic overprinting on apatite U–Th–Pb systems.

Collectively, the hydrothermal apatite U–Th–Pb ages of 150–140 Ma obtained in this study likely represent the timing of Carlin-type gold mineralization in the Youjiang basin. The highly reproducible U–Th–Pb ages of hydrothermal apatite from five different deposits with variable host rocks and mineralization styles attest to the quality and reliability of our dating. These ages are in good agreement within errors with those of in situ SIMS dating on hydrothermal rutile and monazite intergrown with gold-bearing pyrite from the Badu deposit (~ 144 Ma; Gao et al. 2021), and on hydrothermal apatite from the Nibao deposit (~ 142 Ma; Chen et al. 2019), suggesting that these deposits formed nearly synchronously within a narrow time window. On the other hand, it is also noticed that hydrothermal rutile intergrown with gold-bearing sulfides and sericite from the Zhesang deposit in the southern part of the basin has yielded a U–Pb age of 213.6 ± 5.4 Ma (Pi et al. 2017). Therefore, these

recent in situ dating results are suggestive of two episodes of gold mineralization in the Youjiang basin. However, our data suggest that the Early Cretaceous represents the main episode of gold mineralization, because the Shuiyindong, Jinfeng, Zimudang, and Nibao deposits with the 150–140 Ma age range account for over two-thirds of the total gold reserves in the Youjiang basin.

Geodynamic setting of the Carlin-type gold deposits in the Youjiang basin

During the Mesozoic, the Youjiang basin is far away from the active continental margins of South China, making it difficult to identify the tectonic event that has triggered the Carlin-type gold mineralization in the basin. Our new age data of high quality and reliability suggest that the gold mineralization mainly formed at ca. 150–140 Ma, allowing the correlation to the geodynamic framework.

The Mid-Late Jurassic to Early Cretaceous is an important period for the tectono-magmatic evolution of South China. During the Middle Jurassic, the oblique subduction of the Izanagi plate or Paleo-Pacific plate changed the dominant tectonic regime of South China from a Tethyan domain to a Pacific domain (Maruyama et al. 1997; Zhang et al. 2009, 2012; Li et al. 2014; Dong et al. 2015). As subduction continued, a slab window or slab breakup was assumed to have formed in the inland of South China, e.g., the Nanling and Jiangnan regions, during the Late Jurassic to Early Cretaceous. Asthenospheric upwelling resulted in extensive intracrustal remelting, forming metaluminous granitic magmatism with ages of 160–140 Ma in the Nanling and Jiangnan regions (Mao et al. 2013, 2020, 2021). Such a geodynamic mechanism is broadly considered to have triggered the widespread metallogenetic event in the interior of South China, which extends inland for up to 1000 km from the eastern continental margin (Hu and Zhou 2012; Mao et al. 2013). Of particular importance are the world-class granite-related Nanling W–Sn province and the Jiangnan W belt (Fig. 11; Hu and Zhou 2012; Mao et al. 2013, 2020; Hu et al. 2017).

The mineralization ages of these granite-related W–Sn deposits have been well constrained by molybdenite

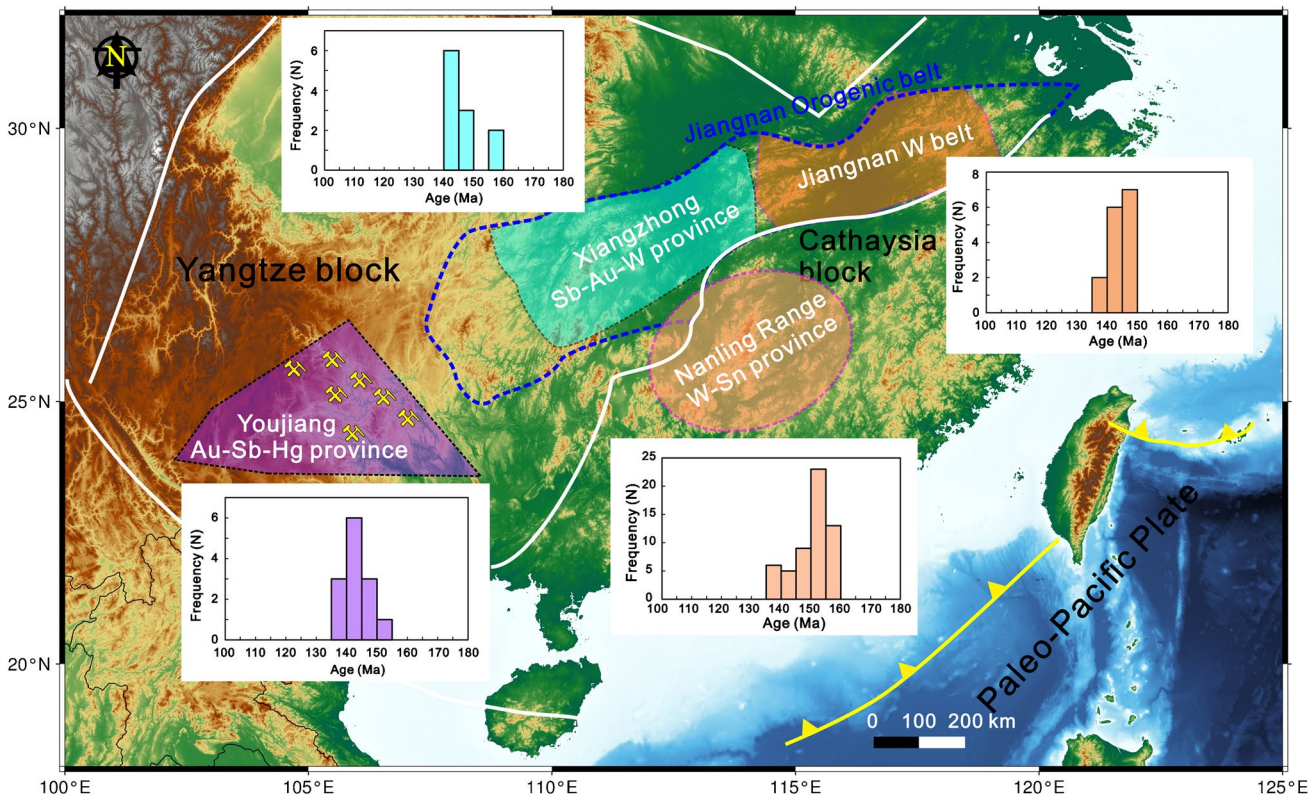

Fig. 11 Age summaries of the Carlin-type gold deposits in the Youjiang basin and W–Sn metallogenesis in South China during the Late Jurassic to Early Cretaceous. The Carlin-type gold deposits temporally overlap with the Xiangzhong Sb–Au–W province, Jiangnan W belt, and Nanling W–Sn province. The data sources of the Youjiang basin are from Chen et al. (2019), Gao et al. (2021), Jin et al. (2021), and this study. The data sources of the Xiangzhong district are from Peng et al. (2003), Xu et al. (2017), Li et al. (2022), and Dai et al. (2022); for the Jiangnan W belt are from Mao et al. (2020, and reference therein) and Song et al. (2021, and reference therein), for the Nanling W–Sn province are from Mao et al. (2013, and reference therein), Gao et al. (2021, and reference therein), and Bai et al. (2022)

Re–Os, muscovite ^{40}Ar–^{39}Ar, and cassiterite, wolframite, and scheelite U–Pb dating techniques, defining 160–138 Ma for the Nanling W–Sn province (Mao et al. 2013; Gao et al. 2021; Bai et al. 2022, and references therein), and 150–137 Ma for the Jiangnan W belt (Mao et al. 2020; Song et al. 2021, and references therein). Recently, the ca. 155–140 Ma metallogenesis is also identified by scheelite and apatite U–Pb dating for the Xiangzhong Sb–Au–W province (Fig. 10; Li et al. 2022; Dai et al. 2022), which is adjacent to the Youjiang basin. Although the Youjiang basin was more continent inward, some igneous rocks with ages of 160–136 Ma were recently reported within and around the basin (ESM 4 Table A4; Li et al. 2013; Zhu et al. 2016; Gan et al. 2020; Su et al. 2021). The mineralization ages of ca. 150–140 Ma for the Carlin-type gold deposits coincide well with the large-scale W–Sn metallogenesis to the east of the basin. Considering this, the Carlin-type gold deposits in the Youjiang basin, therefore, likely share the same geodynamic setting as the W–Sn deposits, both which were triggered by the subduction of the Paleo-Pacific plate (Hu et al. 2017).

Hydrothermal apatite as a potential chronometer for sedimentary rock-hosted gold mineralization

Sedimentary rock-hosted gold deposits are mainly hosted in Ca- and carbonaceous matter-rich carbonate rocks and calcareous siliciclastic rocks (Cline et al. 2005; Goldfarb and Groves 2015; Wu et al. 2020), which provide a substantial reservoir Ca and P for hydrothermal apatite formation. Recently, studies have shown that hydrothermal apatite can indeed form during fluid-rock interaction in sedimentary-hosted gold deposits worldwide (Vielreicher et al. 2010; Chen et al. 2019, 2022; McDivitt et al. 2022; Zhao et al. 2022; Li et al. 2022; this study). Because of the close textural and temporal relationships with gold-bearing sulfides, hydrothermal apatite can represent the timing of gold mineralization. Importantly, hydrothermal apatite has generally large size (tens to hundreds of micrometers) and contains low to high lattice-bound U and Th contents at the μg/g level, making it feasible for in situ U–Th–Pb dating with routine and rapid LA-ICP-MS methods (Chen et al. 2019, 2022; Fox et al. 2021; Ma et al. 2021; Zhao et al. 2022; Li et al. 2022).

Apatite displays highly heterogenous distributions of U and Th contents, which are positively correlated with Na, Y, and REE elements. Combining LA-ICP-MS element mapping with CL imaging can target apatite grains or zones with variable U contents and f_{206} values prior to dating and avoid zones of post-crystallization alteration and metasomatic processes, which is crucial for reliable U–Th–Pb dating.

Conclusions

Hydrothermal apatite coeval with gold mineralization has been identified in five representative Carlin-type gold deposits in the Youjiang basin, by integrating paragenetic, textural, and compositional data. In situ SIMS analysis on hydrothermal apatite from these deposits yields precise and indistinguishable U–Th–Pb ages of 141.0 ± 4.6 Ma to 150.3 ± 6.3 Ma (2σ), representing the timing of the Carlin-type gold deposits in the Youjiang basin. This age range temporally overlaps the widespread granite magmatism and related W–Sn metallogenesis to the east of the Youjiang basin, indicating that they probably share a similar geodynamic setting, driven by asthenospheric upwelling related to the breakup of subducted Paleo-Pacific slab.

Timing constraints on calcareous sedimentary rock-hosted gold deposits are commonly compromised by the lack of routine minerals that are suitable for isotopic dating. Given that hydrothermal apatite is an ubiquitous phosphate mineral in these systems, our case study demonstrates that hydrothermal apatite is a potential robust geochronometer for precisely dating such gold deposits worldwide, provided that the heterogeneous distribution of U, Th, and Pb in hydrothermal apatite is carefully studied prior to dating.

Supplementary Information The online version contains supplementary material available at https://doi.org/10.1007/s00126-023-01196-6.

Acknowledgements Mr. Yu Liu, Ms. Xiaoxiao Ling, Ms. Jiao Li, and Ms. Hongxia Ma are gratefully acknowledged for their laborious works during sample preparations and SIMS analysis. We are grateful to Ms. Zhihui Dai and Mr. Yanwen Tang for help with LA-ICP-MS analysis, respectively. We also would like to thank Chengfu Yang, Lulin Zheng, Baoxian Liu, Jianwen Ma, and Qiang Zhao for their help during field work. Professors Chusi Li from the Indiana University is thanked for giving constructive suggestions that have greatly strengthened this paper. Constructive comments and suggestions from Prof. Bernd Lehmann and anonymous reviewers significantly improved this manuscript.

Funding This work was financially supported by the National Key R&D Program (2018YFA0702600) and the National Natural Science Foundation of China (42103067, 41830432, U1812402).

Declarations

Conflict of interest The authors declare no competing interests.

References

Andersson SS, Wagner T, Jonsson E, Fusswinkel T, Whitehouse MJ (2019) Apatite as a tracer of the source, chemistry and evolution of ore-forming fluids: the case of the Olserum-Djupedal REE-phosphate mineralization, SE Sweden. Geochim Cosmochim Acta 255:163–187

Arehart GB, Foland KA, Naeser CW, Kesler SE (1993) $^{40}Ar/^{39}Ar$, K/Ar, and fission track geochronology of sediment-hosted disseminated gold deposits at Post-Betze, Carlin trend, northeastern Nevada. Econ Geol 88:622–646

Arehart GB, Chakurian AM, Tretbar DR, Christensen JN, McInnes BR, Donelick RA (2003) Evaluation of radioisotope dating of Carlin-type deposits in the Great Basin, western North America, and implications for deposit genesis. Econ Geol 98:235–248

Bai XJ, Liu M, Yu RG, Fang Y, Liu X, Tang B, Qiu HN (2022) Well-constrained mineralization ages by integrated $^{40}Ar/^{39}Ar$ and U-Pb dating techniques for the Xitian W-Sn polymetallic deposit, South China. Econ Geol 117:833–852

Barker SLL, Hickey KA, Cline JS, Dipple GM, Kilburn MR, Vaughan JR, Longo AA (2009a) Uncloaking invisible gold: use NanoSIMS to evaluate gold, trace elements, and sulfur isotopes in pyrite from Carlin-type gold deposits. Econ Geol 104:897–904

Barker SLL, Hickey KA, Dipple GM, Layne G (2009b) Apatite as a paleohydrothermal fluid recorder in Carlin-type gold deposits. American Geophysical Union Joint Assembly 2009, Spring Meeting Abstracts, Toronto, Canada

Cai JX, Zhang KJ (2009) A new model for the Indochina and South China collision during the Late Permian to the Middle Triassic. Tectonophysics 467:35–43

Cao MJ, Evans NJ, Hollings P, Cooke DR, McInnes BIA, Qin KZ (2021) Apatite texture, composition, and O-Sr-Nd isotope signatures record magmatic and hydrothermal fluid characteristics at the Black Mountain porphyry deposit, Philippines. Econ Geol 116:1189–1207

Chakurian AM, Arehart GB, Donelick RA, Zhang X, Reiners PW (2003) Timing constraints of gold mineralization along the Carlin trend utilizing apatite fission track, $^{40}Ar/^{39}Ar$, and apatite (U-Th)/He methods. Econ Geol 98:1159–1171

Chen MH, Huang QW, Hu Y, Chen ZY, Zhang W (2009) Genetic types of phyllosilicate (micas) and its $^{39}Ar/^{40}Ar$ dating in Lannigou gold deposit, Guizhou Province, China. Acta Mineral Sin 29:353–362 (in Chinese with English abstract)

Chen MH, Mao JW, Bierlein FP, Norman T, Uttley PJ (2011) Structural features and metallogensis of the Carlin-type Jinfeng (Lannigou) gold deposit, Guizhou Province, China. Ore Geol Rev 43:217–234

Chen MH, Mao JW, Li C, Zhang ZQ, Dang Y (2015) Re-Os isochron ages for arsenopyrite from Carlin-like gold deposits in the Yunnan-Guizhou-Guangxi "golden triangle", southwestern China. Ore Geol Rev 64:316–327

Chen J, Yang RD, Du LJ, Zheng LL, Gao JB, Lai CK, Wei HR, Yuan MG (2018) Mineralogy, geochemistry and fluid inclusions of the Qinglong Sb-(Au) deposit, Youjiang basin (Guizhou, SW China). Ore Geol Rev 92:1–18

Chen MH, Bagas L, Liao X, Zhang ZQ, Li QL (2019) Hydrothermal apatite SIMS Th-Pb dating, constrains on the timing of low temperature hydrothermal Au deposit in Nibao, SW China. Lithos 324–325:418–428

Chen HJ, Sun XM, Li DF, Yin R, Tong ZD, Wu ZW, Fu Y, Liu QF, Chen X, Yi JZ, Deng XG (2022) In situ apatite U-Pb dating for the ophiolite-hosted Nianzha orogenic gold deposit, Southern Tibet. Ore Geol Rev 144:104811

Cherniak DJ (2010) Diffusion in accessory minerals: zircon, titanite, apatite, monazite and xenotime. Rev Miner Geochem 72:827–869

Cherry AR, Kamenetsky VS, McPhie J, Thompson JM, Ehrig K, Meffre S, Kamenetsky MB, Krneta S (2018) Tectonothermal events in the Olympic IOCG province constrained by apatite and REE phosphate geochronology. Austral J Earth Sci 65:1–17

Chew DM, Spikings RA (2015) Geochronology and thermochronology using apatite: time and temperature, lower crust to surface. Elements 11:189–194

Chew DM, Sylvester PJ, Tubrett MN (2011) U-Pb and Th-Pb dating of apatite by LA-ICPMS. Chem Geol 280:200–216

Chew DM, Petrus JA, Kamber BS (2014) U-Pb LA-ICPMS dating using accessory mineral standards with variable common Pb. Chem Geol 363:185–199

China Geological Survey (2015) Discovery of large gold deposits in the Jinya deposit. Guangxi Gold Sci Tech 23:54 (in Chinese with English abstract)

Cline JS (2001) Timing of gold and arsenic sulfide mineral deposition at the Getchell Carlin-type gold deposit, north-central Nevada. Econ Geol 96:75–89

Cline JS (2018) Nevada's Carlin-type gold deposits, what we've learned during the past 10 to 15 years. Rev Econ Geol 20:7–37

Cline JS, Hofstra AH, Muntean JL, Tosdal RM, Hickey KA (2005) Carlin-type gold deposits in Nevada: critical geologic characteristics and viable models. In: Hedenquist JW, Thompson JFH, Goldfarb RJ, Richards JP (eds) Economic Geology 100th Anniversary Volume. Society of Economic Geologists, Littleton, Colorado, pp 451–484

Cochrane R, Spikings RA, Chew D, Wotzlaw JF, Chiaradia M, Tyrrell S, Schaltegger U, Lelij RVd (2014) High temperature (>350°C) thermochronology and mechanisms of Pb loss in apatite. Geochim Cosmochim Acta 127:39–56

Dai JF, Xu DR, Chi GX, Li ZH, Deng T, Zhang J, Li B (2022) Origin of the Woxi orogenic Au-Sb-W deposit in the west Jiangnan Orogen of South China: constraints from apatite and wolframite U-Pb dating and pyrite in-situ S-Pb isotopic signatures. Ore Geol Rev 150:105134

Dong SW, Zhang YQ, Zhang FQ, Cui JJ, Chen XH, Zhang SH, Miao LC, Li JH, Shi W, Li ZH, Huang SQ, Li HL (2015) Late Jurassic-Early Cretaceous continental convergence and intracontinental orogenesis in East Asia: a synthesis of the Yanshan Revolution. J Asian Earth Sci 114:750–770

Du YS, Huang H, Yang JH, Huang HW, Tao P, Huang ZQ, Hu LS, Xie CX (2013) The basin translation from Late Paleozoic to Triassic of the Youjiang basin and its tectonic signification. Geol Rev 59:1–11 (in Chinese with English abstract)

Ehrig K, Kamenetsky VS, McPhie J, Macmillan E, Thompson J, Kamenetsky M, Maas R (2021) Staged formation of the supergiant Olympic Dam uranium deposit, Australia. Geology 49:1312–1316

Eldorado Gold Corporation (2011) Technical report for the Jinfeng goldmine, China. www.eldoradogold.com/i/pdf/TechRptJinfeng_Mine.pdf

Fan WM, Zhang CH, Wang YJ, Guo F, Peng TP (2008) Geochronology and geochemistry of Permian basalts in western Guangxi Province, Southwest China: evidence for plume-lithosphere interaction. Lithos 102:218–236

Fox DCM, Spinks SC, Barham M, Kirkland CL, Pearce MA, Aspandiar M, Birchall R, Mead E (2021) Working up an apatite: enigmatic Mesoarchean hydrothermal Cu-Co-Au mineralization in the Pilbara Craton. Econ Geol 116:1561–1573

Gan CS, Wang YJ, Barry TL, Zhang YZ, Qian X (2020) Late Jurassic high-Mg andesites in the Youjiang Basin and their significance for the southward continuation of the Jiangnan Orogen, South China. Gondwana Res 77:260–273

Gao W, Hu RZ, Hofstra AH, Li QL, Zhu JJ, Peng KQ, Mu L, Huang Y, Ma JW, Zhao Q (2021) U-Pb dating on hydrothermal rutile and monazite from the Badu gold deposit supports an Early Cretaceous age for Carlin–type gold mineralization in the Youjiang Basin, Southwestern China. Econ Geol 116:1355–1385

Gao W, Hu RZ, Mei L, Bi XW, Fu SL, Huang ML, Yan J, Li JW (2022) Monitoring the evolution of sulfur isotope and metal concentrations across gold-bearing pyrite of Carlin-type gold deposits in the Youjiang Basin, SW China. Ore Geol Rev 147:104990

Ge X, Selby D, Liu JJ, Chen YZ, Cheng GF, Shen CB (2021) Genetic relationship between hydrocarbon system evolution and Carlin-type gold mineralization: insights from Re-Os pyrobitumen and pyrite geochronology in the Nanpanjiang Basin, South China. Chem Geol 559:119953

Goldfarb RJ, Groves DI (2015) Orogenic gold: Common or evolving fluid and metal sources through time. Lithos 233:2–26

Gu XX, Zhang YM, Li BH, Dong SY, Xue CJ, Fu SH (2012) Hydrocarbon and ore-bearing basinal fluids: a possible link between gold mineralization and hydrocarbon accumulation in the Youjiang basin, South China. Miner Deposita 47:663–682

Harlov DE (2015) Apatite: a fingerprint for metasomatic processes. Elements 11:171–176

Hill TJ (2016) Time-space relationships between sediment-hosted gold mineralization and intrusion-related polymetallic mineralization at Kinsley Mountain, Nevada. Dissertation, University of Nevada (Reno)

Hofstra AH, Snee LW, Rye RO, Folger HW, Phinisey JD, Loranger RJ, Dahl AR, Naeser CW, Stein HJ, Lewchuk M (1999) Age constraints on Jerritt Canyon and other Carlin-type gold deposits in the western United States-relationship to Mid-Tertiary extension and magmatism. Econ Geol 94:769–802

Hou L, Peng HJ, Ding J, Zhang JR, Zhu SB, Wu SY, Wu Y, Ouyang HG (2016) Textures and in situ chemical and isotopic analyses of pyrite, Huijiabao trend, Youjiang basin, China: Implications for paragenesis and source of sulfur. Econ Geol 111:331–353

Hu RZ, Zhou MF (2012) Multiple Mesozoic mineralization events in South China-an introduction to the thematic issue. Miner Deposita 47:579–588

Hu RZ, Su WC, Bi XW, Tu GZ, Hofstra AH (2002) Geology and geochemistry of Carlin-type gold deposits in China. Miner Deposita 37:378–392

Hu RZ, Fu SL, Huang Y, Zhou MF, Fu SH, Zhao CH, Wang YJ, Bi XW, Xiao JF (2017) The giant South China Mesozoic low-temperature metallogenic domain, reviews and a new geodynamic model. J Asian Earth Sci 137:9–34

Hu RZ, Wen HJ, Ye L, Chen W, Xia Y, Fan HF, Huang Y, Zhu JJ, Fu SL (2020) Metallogeny of critical metals in the Southwestern Yangtze Block. Chin Sci Bull 65:3700–3714 (in Chinese with English abstract)

Huang Y (2019) Mineralization age and material source of the Carlin-type gold deposits in Southwestern Guizhou. Dissertation, Institute of Geochemistry, Chinese Academy of Sciences (Guiyang)

Huang Y, Hu RZ, Bi XW, Fu SL, Peng KQ, Gao W, Oyebamiji A, Zhaanbaeva A (2019) Low-temperature thermochronology of the Carlin-type gold deposits in southwestern Guizhou, China: Implications for mineralization age and geological thermal events. Ore Geol Rev 115:103178

Hutcherson S (2002) Geology and geochemistry of the Murray deposit, Jerritt Canyon mining district, Nevada. Dissertation, University of Nevada (Reno)

Ilchick RP, Uttley PJ, Corben R, Zhang AY, Ham A, Hodkiewicz P (2005) The Jinfeng gold deposit: mining the new frontier of China. in Rhoden HN, Steininger RC, Vikre PG (eds) Window to the world: 2005 Symposium proceedings: Reno, Nevada, Geological Society of Nevada, pp 887–898

Jin XY, Zhao JX, Feng YX, Hofstra AH, Deng XD, Zhao XF, Li JW (2021) Calcite U-Pb dating unravels the age and hydrothermal history of the giant Shuiyindong Carlin-type gold deposits in the golden triangle, South China. Econ Geol 116:1253–1265

Kirkland CL, Yakymchuk C, Szilas K, Evans N, Hollis J, McDonald B, Gardiner NJ (2018) Apatite: a U-Pb thermochronometer or geochronometer? Lithos 318–319:143–157

Li QL, Li XH, Wu FY, Yin QZ, Ye HM, Liu Y, Tang GQ, Zhang CL (2012) In-situ SIMS U-Pb dating of phanerozoic apatite with low U and high common Pb. Gondwana Res 21:745–756

Li JK, Wang DH, Li HQ, Chen ZH, Mei YP (2013) Late Jurassic-Early Cretaceous mineralization in the Laojunshan ore concentration area, Yunnan province. Earth Sci 38:1023–1036 (in Chinese with English abstract)

Li JH, Zhang YQ, Dong SW, Johnston ST (2014) Cretaceous tectonic evolution of South China: a preliminary synthesis. Earth-Sci Rev 134:98–136

Li JX, Hu RZ, Zhao CH, Zhu JJ, Huang Y, Gao W, Li JW, Zhuo YZ (2020) Sulfur isotope and trace element compositions of pyrite determined by NanoSIMS and LA-ICP-MS: new constraints on the genesis of the Shuiyindong Carlin-like gold deposit in SW China. Miner Deposita 55:1279–1298

Li W, Xie GQ, Mao JW, Cook NJ, Wei HT, Ji YH, Fu B (2022) Precise age constraints for the Woxi Au-Sb-W deposit, South China. Econ Geol 118:509–518

Liang QL, Xie ZJ, Song XY, Wirth R, Xia Y, Cline J (2021) Evolution of invisible Au in arsenian pyrite in Carlin-type Au deposits. Econ Geol 116:515–526

Liu JZ, Deng YM, Liu CQ, Zhang XC, Xia Y (2006) Metallogenic conditions and model of the super-large Shuiyindong stratabound gold deposit in Zhenfeng County, Guizhou Province. Geol China 33:169–177 (in Chinese with English abstract)

Liu S, Su WC, Hu RZ, Feng CX, Gao S, Coulson IM, Wang T, Feng GY, Tao Y, Xia Y (2010) Geochronological and geochemical constraints on the petrogenesis of alkaline ultramafic dykes from southwest Guizhou Province, SW China. Lithos 114:253–264

Lubben JD, Cline JS, Barker SLL (2012) Ore fluid properties and sources from quartz-associated gold at the Betze-Post Carlin-type gold deposit, Nevada, United States. Econ Geol 107:1351–1385

Ma Y, Jiang SY, Frimmel HE, Xiong SF, Zhu LY, Chen RS (2021) Early Paleozoic orogenic gold deposit in the Cathaysia Block, China: a first example from the Shuangqishan deposit. Gondwana Res 91:231–253

Mao JW, Cheng YB, Chen MH, Pirajno F (2013) Major types and time-space distribution of Mesozoic ore deposits in South China and their geodynamic settings. Miner Deposita 48:267–294

Mao M, Rukhlov AS, Rowins SM, Spence J, Coogan LA (2015) Apatite trace element compositions: a robust new tool for mineral exploration. Econ Geol 111:1187–1222

Mao JW, Wu SH, Song SW, Dai P, Xie GQ, Su QW, Liu P, Wang XG, Yu ZX, Chen XY, Tang WX (2020) The world-class Jiangnan tungsten belt: geological characteristics, metallogeny, and ore deposit model. Chin Sci Bull 65:3746–3762

Mao JW, Zhang W, Xie GQ, Lehmann B, Goldfarb RJ (2021) Recognition of a Middle-Late Jurassic arc-related porphyry copper belt along the southeast China coast: geological characteristics and metallogenic implications. Geology 49:592–596

Maruyama S, Isozaki Y, Kimura G, Terabayashi M (1997) Paleogeographic maps of the Japanese Islands: plate tectonic synthesis from 750 Ma to the present. Island Arc 6:121–142

McDivitt JA, Hagemann SG, Kemp AIS, Thébaud N, Fisher CM, Rankenburg K (2022) U-Pb and Sm-Nd evidence for episodic Orogenic gold mineralization in the Kalgoorlie gold camp, Yilgarn craton, Western Australia. Econ Geol 117:747–775

Muntean JL, Cline JS (2018) Diversity of Carlin-type gold deposits. Rev Econ Geol 20:1–5

O'Sullivan G, Chew D, Kenny G, Henrichs I, Mulligan O (2020) The trace element composition of apatite and its application to detrital provenance studies. Earth Sci Rev 201:103044

Palenik CS, Utsunomiya S, Reich M, Kesler SE, Wang LM, Ewing RC (2004) "Invisible" gold revealed: direct imaging of gold nanoparticles in a Carlin-type deposit. Am Miner 89:1359–1366

Palma G, Barra F, Reich M, Valencia V, Simon AC, Vervoort J, Leisen M, Romero R (2019) Halogens, trace element concentrations, and Sr-Nd isotopes in apatite from iron oxide-apatite (IOA)

deposits in the Chilean iron belt: evidence for magmatic and hydrothermal stages of mineralization. Geochim Cosmochim Acta 246:515–540

Pan Y, Fleet ME (2002) Compositions of the apatite-group minerals: substitution mechanisms and controlling factors. Rev Miner Geochem 48:13–49

Peng JT, Hu RZ, Burnard PG (2003) Samarium-neodymium isotope systematics of hydrothermal calcites from the Xikuangshan antimony deposit (Hunan, China): the potential of calcite as a geochronometer. Chem Geol 200:129–136

Pi QH, Hu RZ, Xiong B, Li QL, Zhong RC (2017) In situ SIMS U-Pb dating of hydrothermal rutile, reliable age for the Zhesang Carlin-type gold deposit in the golden triangle region, SW China. Miner Deposita 52:1179–1190

Qiu L, Yan DP, Tang SL, Wang Q, Yang WX, Tang XL, Wang JB (2016) Mesozoic geology of southwestern China: Indosinian foreland overthrusting and subsequent deformation. J Asian Earth Sci 122:91–105

Rasmussen B, Sheppard S, Fletcher IR (2006) Testing ore deposit models using in situ U-Pb geochronology of hydrothermal monazite, Paleoproterozoic gold mineralization in northern Australia. Geology 34:77–80

Reich M, Kesler SE, Utsunomiya S, Palenik CS, Chryssoulis SL, Ewing RC (2005) Solubility of gold in arsenian pyrite. Geochim Cosmochim Acta 69:2781–2796

Simon G, Kesler SE, Chryssoulis S (1999) Geochemistry and texture of gold-bearing arsenian pyrite, Twin Creeks, Nevada: implication for deposition of gold in Carlin-type deposit. Econ Geol 94:405–421

Song SW, Mao JW, Xie GQ, Lehmann B, Jian W, Wang XG (2021) The world-class mid-Mesozoic Jiangnan tungsten belt, South China: coeval large reduced and small oxidized tungsten systems controlled by different magmatic petrogenesis. Ore Geol Rev 139:104543

Stacey JS, Kramers JD (1975) Approximation of terrestrial lead isotope evolution by a two-stage model. Earth Planet Sci Lett 26:207–221

Su WC, Heinrich CA, Pettke T, Zhang XC, Hu RZ, Xia B (2009a) Sediment-hosted gold deposits in Guizhou, China, products of wall-rock sulfidation by deep crustal fluids. Econ Geol 104:73–93

Su WC, Hu RZ, Xia B, Xia Y, Liu YP (2009b) Calcite Sm-Nd isochron age of the Shuiyindong Carlin-type gold deposit, Guizhou, China. Chem Geol 258:269–274

Su WC, Zhang HT, Hu RZ, Ge X, Xia B, Chen YY, Zhu C (2012) Mineralogy and geochemistry of gold-bearing arsenian pyrite from the Shuiyindong Carlin-type gold deposit, Guizhou, China, implications for gold depositional processes. Miner Deposita 47:653–662

Su WC, Dong WD, Zhang XC, Shen NP, Hu RZ, Hofstra AH, Cheng LZ, Xia Y, Yang KY (2018) Carlin-type gold deposits in the Dian-Qian-Gui "Golden Triangle" of Southwest China. Rev Econ Geol 20:157–185

Su HM, Jiang SY, Shao JB, Zhang DY, Wu XK, Huang XQ (2021) New identification and significance of Early Cretaceous mafic rocks in the interior South China Block. Scie Rep 11:11396

Sun SS, McDonough WF (1989) Chemical and isotopic systematics of oceanic basalts: implications for mantle composition and processes. Geol Soc Lond Spec Publ 42:313–345

Tan QP, Xia Y, Xie ZJ, Yan J (2015) Migration paths and precipitation mechanisms of ore-formation fluid at the Shuiyindong Carlin-type gold deposit, Guizhou, China. Ore Geol Rev 69:140–156

Thompson J, Meffre S, Maas R, Kamenetsky V, Kamenetsky M, Goemann K, Ehrig K, Danyushevsky L (2016) Matrix effects in Pb/U measurements during LA-ICP-MS analysis of the mineral apatite. J Anal Atom Spectrom 31:1206–1215

Thomson SN, Gehrels GE, Ruiz J, Buchwaldt R (2012) Routine low-damage apatite U-Pb dating using laser ablation-multicollector-ICPMS. Geochem Geophys Geosyst 13:Q0AA21

Tretbar D, Arehart GB, Christensen JN (2000) Dating gold deposition in a Carlin-type gold deposit using Rb/Sr methods on the mineral galkhaite. Geology 28:947–950

Ulrich T, Kamber BS, Jugo PJ, Tinkham DK (2009) Imaging element distribution patterns in minerals by laser ablation-inductively coupled plasma-mass spectrometry (LA-ICP-MS). Can Miner 47:1001–1012

Vielreicher NM, Groves DI, Snee LW, Fletcher IR, McNaughton NJ (2010) Broad synchroneity of three gold mineralization styles in the Kalgoorlie gold field: SHRIMP, U-Pb, and $^{40}Ar/^{39}Ar$ geochronological evidence. Econ Geol 105:187–227

Wang QF, Yang L, Xu XJ, Santosh M, Wang YN, Wang TY, Chen FG, Wang RX, Gao L, Liu XF, Yang SJ, Zeng YS, Chen JH, Zhang QZ, Deng J (2020) Multi-stage tectonics and metallogeny associated with Phanerozoic evolution of the South China Block: a holistic perspective from the Youjiang basin. Earth Sci Rev 211:103405

Wu YF, Evans K, Fisher LA, Zhou MF, Hu SY, Fougerouse D, Large RR, Li JW (2020) Distribution of trace elements between carbonaceous matter and sulfides in a sediment-hosted orogenic gold system. Geochim Cosmochim Acta 276:345–362

Xie ZJ, Xia Y, Cline JS, Koenig A, Wei DT, Tan QP, Wang ZP (2018) Are there Carlin-type gold deposits in China? A comparison of the Guizhou, China, deposits with Nevada, USA, deposits. Rev Econ Geol 20:187–233

Xu DR, Deng T, Chi GX, Wang ZL, Zou FH, Zhang JL, Zou SH (2017) Gold mineralization in the Jiangnan orogenic belt of South China: geological, geochemical and geochronological characteristics, ore deposit-type and geodynamic setting. Ore Geol Rev 88:565–618

Yan DP, Zhou MF, Wang YC, Xia B (2006) Structural and geochronological constraints on the tectonic evolution of the Dulong-Song Chay tectonic dome in Yunnan province, SW China. J Asian Earth Sci 28:332–353

Yang JH, Cawood PA, Du YS, Huang H, Hu LS (2012) Detrital record of Indosinian mountain building in SW China: provenance of the Middle Triassic turbidites in the Youjiang Basin. Tectonophysics 574–575:105–117

Yang WX, Yan DP, Qiu L, Wells ML, Dong JM, Gao T, Zhang Z, Mu HX, Wang XW, Wang FY (2021) Formation and forward propagation of the Indosinian foreland fold-thrust belt and Nanpanjiang foreland basin in SW China. Tectonics 40:e2020TC006552

Yang L, Wang QF, Large RR, Fougerouse D, Mukherjee I, Zhang QZ, Deng J (2022) Texture and geochemistry of pyrite from the Jinya, Nakuang and Gaolong gold deposits in the Youjiang Basin: implications for basin-scale gold mineralization. Miner Deposita 57:1367–1390

Zhang F, Yang KY (1992) Using quartz fission track ages to constrain the timing of fine disseminated gold deposit in southwestern Guizhou. Chin Sci Bull 37:1593–1595 (in Chinese)

Zhang XC, Spiro B, Halls C, Stanley CJ, Yang KY (2003) Sediment-hosted disseminated gold deposits in Southwest Guizhou, PRC: their geological setting and origin in relation to mineralogical, fluid inclusion, and stable-isotope characteristics. Inter Geol Rev 45:407–470

Zhang YQ, Xu XB, Jia D, Shu LS (2009) Deformation record of the change from Indosinian collision-related tectonic system to Yanshanian subduction-related tectonic system in South China during the Early Mesozoic. Earth Sci Front 16:234–247 (in Chinese with English abstract)

Zhang YQ, Dong SW, Li JH, Cui JJ, Shi W, Su JB, Li Y (2012) The new progress in the study of Mesozoic tectonics of South China. Acta Geosci Sin 33:257–279

Zhao JH, Zhou MF, Yan DP, Zheng JP, Li JW (2011) Reappraisal of the ages of Neoproterozoic strata in South China: no connection with the Grenvillian orogeny. Geology 39:299–302

Zhao XF, Zhou MF, Gao JF, Li XC, Li JW (2015) In situ Sr isotope analysis of apatite by LA-MC-ICPMS: constraints on the evolution of ore fluids of the Yinachang Fe-Cu-REE deposit, Southwest China. Miner Deposita 50:871–884

Zhao SR, Li JW, McFarlane CRM, Robinson PT, Li ZK, Wu YF, Zhao XF, He CG, Kang X, Chen CY (2022) Recognition of late Paleoproterozoic gold mineralization in the North China craton: evidence from multi-mineral U-Pb geochronology and stable isotopes of the Shanggong deposit. Geol Soc Am Bull. https://doi.org/10.1130/B362811

Zhou MF, Zhao JH, Qi L (2006) Zircon U-Pb geochronology and elemental and Sr-Nd isotopic geochemistry of Permian mafic rocks in the Funing area, SW China. Contrib Miner Petrol 151:1–19

Zhu JJ, Zhong H, Xie GQ, Zhao CH, Xu LL, Lu G (2016) Origin and geological implication of the inherited zircon from felsic dykes, Youjiang basin, China. Acta Petrol Sin 32:3269–3280 (in Chinese with English abstract)

Zhuo YZ, Hu RZ, Xiao JF, Zhao CH, Huang Y, Yan J, Li JW, Gao W, Li JX (2019) Trace elements and C-O isotopes of calcite from Carlin-type gold deposits in the Youjiang Basin, SW China: constraints on ore-forming fluid compositions and sources. Ore Geol Rev 113:103067